CFD-based prediction of initial microalgae adhesion to solid surfaces using force balances

S. Kichouh-Aiadi, A. Sánchez-Mirón[*], J.J. Gallardo-Rodríguez, Y. Soriano-Jerez, M.C. Cerón-García, F. García-Camacho, E. Molina Grima

Department of Chemical Engineering, Research Centre CIAMBITAL, University of Almería, 04120 Almería, Spain

*Corresponding author: Telephone: +34 950 214025; fax: 34 950 015491

E-mail address: asmiron@ual.es

1

Abstract

Adhesion of microalgal cells to photobioreactor walls reduces productivity resulting in significant economic losses. The physicochemical surface properties and the fluid dynamics present in the photobioreactor during cultivation are relevant. However, to date, no multiphysical model has been able to predict biofouling formation in these systems. In this work, to model the microalgae adhesion, a computational fluid-dynamic simulation has been performed using a Eulerian-Lagrangian particle-tracking model. The adhesion criterion was based on the balance of forces and moments included in the XDLVO model. A cell suspension of the marine microalgae *Nannochloropsis gaditana* was fed into a commercial flow cell composed of poly-methyl-methacrylate coupons for validation. Overall, the simulated adhesion criterion qualitatively predicted the initial distribution of adhered cells on the coupons. In conclusion, the combined Computational Fluid Dynamics-Discrete Phase Model (CFD-DPM) approach can be used to overcome the challenge of predicting microalgal cell adhesion in photobioreactors.

Keywords

1. Introduction

Microalgae present highly diverse biochemical compositions, which make them a potentially profitable and sustainable feedstock for biomass production and for commercially attractive compounds such as polysaccharides, lipids, proteins, enzymes, vitamins and carotenoids (Becker 2007; Christaki et al. 2011; Koyande et al. 2019), as well as for biofuels (Chisti 2010). However, there are still important hurdles to overcome before they can be used extensively, as reported in the literature (Norsker et al. 2011; Coons et al. 2014). One of these issues is biofouling formation on the photobioreactor (PBR) surfaces, which severely affects production system performance because light penetration is seriously reduced (Zeriouh et al. 2017).

Moreover, this phenomenon damages the component materials of the PBR, accelerating their deterioration. The effective removal of biofouling in PBRs imposes an economic cost due to the time expended on the cleaning process and the eventual replacement of the transparent material.

PBR biofouling follows a predictable sequence of events (Bos et al. 1999; Talluri et al. 2020): (i) formation of a conditioning layer, which in microalgae is typically made up of polyphenolic compounds and anionic polysaccharides (Vreeland et al. 1998); (ii) formation of a primitive layer of cells that adheres to the PBR surface; (iii) cell colonization and proliferation on the surface. The timescale varies greatly and depends on the type of cells, in certain cases occurring in minutes (Busscher & Van Der Mei 2006; Moreira et al. 2014). The factors related with this phenomenon's appearance are diverse, although the most important is the nature of the cell interaction with the surface and the bioreactor's fluid dynamics (Pereira et al. 2002; Simões et al. 2007; Zeriouh et al. 2017; Zeriouh et al. 2019).

Cell adhesion has been explained as resulting from a balance of forces (Bos et al. 1999; Adamczyk et al. 2000; Pereira et al. 2002), some of them dependant on the flow. Thus, in order to study cell adhesion, it is necessary to know the hydrodynamic conditions; this is why flow devices of different designs are used for biofilm formation studies (Azeredo et al. 2017). The wall shear stress that develops in these systems is representative of the one acting on the curved walls typical in industrial equipment (Teodósio et al. 2012).

Ideally, the flow cell design should allow the fluid flow to develop a steady laminar profile according to Poiseuille's law. One of the key design issues concerns the geometry of the flow cell and the inlet conditions, which dictate the length required for complete flow development (Bakker et al. 2003). Several flow cell designs (Pereira et al. 2002; Dimartino et al. 2014) have been used to test different materials and different flow conditions (Johnston & Jones 1995; Pereira et al. 2002; Moreira et al. 2014; Moreira et al. 2015).

By comparing the deposition rate of well-defined particles on coupons placed inside a flow cell to theoretical predictions, important information can be obtained on the nature of the colloidal and hydrodynamic forces operating at short particle-surface separations (Elimelech 1994). However, microorganisms are chemically more complex than any inert particle and have heterogeneous surface structures. So far, no satisfactory model has been developed that includes flow regimes for cell adhesion on surfaces (Vadillo-Rodríguez et al. 2004; Dimartino et al. 2014).

Some adhesion models are based on thermodynamics; these try to explain adhesion using the concept of surface free energy, without taking electrostatic interactions into account (Bos et al. 1999). Other models are based on the wide range of interaction forces exerted on cells; these can be classified as: interactions between particles, interactions between particles and surfaces, and interactions between particles and the fluid (fluid-

dynamic forces). In this last group, fluid-dynamic forces generally include drag force, lift force, and buoyancy force. Usually, the magnitude of the fluid-dynamic forces needed to prevent adhesion is smaller than the values needed to detach the cells (Boks et al. 2008). Among the models based on the balance of forces, the most used has been the DLVO theory (from the initials of its authors: Derjaguin, Landau, Verwey, and Overbeek), which dates from the 1940s, and its extension, the XDLVO model, introduced by van Oss et al. (van Oss 1993). These explain cell adhesion based on a balance of non-covalent short-range attractive and repulsive forces: Lifshitz-van der Waals, electrostatic, Lewis acid-base, and the Brownian force of motion (Bos et al. 1999). The Basset force, the virtual mass force, the force of Brownian motion and the magnus force are negligible at low fluid velocities, when the particles are small and spherical in shape (Kallio & Reeks 1989; McLaughlin 1989; Zhang & Chen 2009; Barker 2010). Ozkan and Berberoglu demonstrated that the XDLVO model accurately explained the forces responsible for microalgal adhesion to solid surfaces (Ozkan & Berberoglu 2013). The interaction forces, which only exist very close to the wall, are critical, as they determine the onset of biofouling (van Oss 1993; Bos et al. 1999; Zeriouh et al. 2017). Furthermore, the forces change over time because the surface properties also do, being able to increase by several orders of magnitude in just one hour (Dąbroś & Van De Ven 1982).

Computational Fluid Dynamics (CFD) is a tool that has proven useful in accurately characterizing flow cells of different geometries and sizes (Teodósio et al. 2012; Zeriouh et al. 2019) but experimental validation is needed to prove the reliability of the model settings used (Kang et al. 2020).

The Lagrangian-Eulerian (LE) approach may help to reconcile the simulations with the observations. In contrast to other approaches, it can manage a wide range of particle sizes in both diluted and dense particle flows, and captures nonlinear, multiscale

5

interactions as well as non-equilibrium effects (Subramaniam 2013). In Lagrangian tracking, the balance of forces may define the particle's motion and its direction, allowing an individual prediction of the spot where a particle will approach the surface. It has been shown that trajectory analysis offers an alternative for solving the complete convective diffusion equation of non-Brownian particles (Elimelech 1994). In ANSYS software, DPM (Discrete Phase Model) allows individual monitoring of each particle in a set (Ansys Fluent, 2003). Depending on the particle volume fraction, one-way or two-way coupling should be used in the simulations to account for the possible force exerted on the flow by the particles (Greifzu et al. 2016).

In this work, CFD-added cell adhesion simulations were performed using the Eulerian-Lagrangian model for particle tracking in a flow cell of parallel plates containing poly-methyl-methacrylate (PMMA) coupons. The results from the CFD were compared to the experimental observations obtained from the flow cell fed with a suspension of the marine microalgae *Nannochloropsis gaditana*. An adhesion criterion based on the balance of forces and moments was implemented in the XDLVO model to predict the initial adhesion of microalgal cells.

2. Materials and Methods

2.1. Flow cell

A commercial two-channel flow cell was used (FC271 flow cell model, BioSurface Technologies Corporation, Montana, USA) (Figure 1a). It allows one to evaluate three circular coupons in each channel. The coupon dimensions are 10 mm diameter × 2 mm thick. According to the manufacturer, the maximum flow allowed in the channels is 3.5 mL·min^{-1}. The main dimensions of the flow cell are shown in Figures 1b and 1b. The channel is 39.45 mm in length. The coupons are separated from each other by a 2.1 mm central slit. The thickness of the channel is 0.4 mm. The maximum cell width corresponds

6

to the central rectangular section and measures 24.4 mm long and 12.9 mm wide. At the inlet and outlet, there is a triangular constriction to ensure the development of laminar flow (Ozkan & Berberoglu 2013). The experiments were carried out with 3 poly-methyl-methacrylate coupons, a commonly used material in photobioreactor construction.

2.2.   Coupon Surface conditioning

The PMMA coupons (purchased from Talleres Transglass, Ltd., Avilés, Spain) were characterized as previously reported (Ozkan & Berberoglu 2013; Soriano-Jerez et al. 2020). They were cleaned prior to use in the flow cell, as described in Ruiz-Cabello et al. (2011). Briefly, the coupons were first washed with a 1% w/w Alconox solution (Alconox Inc., Alconox, NY, USA) and sonicated (280W, 50Hz) for 10 minutes. Then, they were washed with distilled water and sonicated for a further 5 minutes in hexane. Afterwards, they were washed once more with Mili-Q water and sonicated for another 5 minutes in Mili-Q water. Finally, the coupons were allowed to dry at room temperature.

2.3.   Adhesion assays

Adhesion assays were carried out by recirculating a healthy suspension of the microalga (the culture conditions and protocols are reported elsewhere; López-Rosales et al., (2014)). *Nannochloropsis gaditana* B-3 was obtained from the *Instituto de Ciencias Marinas de Andalucía* (CSIC, Cádiz, Spain). The cell suspension was pumped from a 13-L steady-state (dilution rate of 0.1 day^{-1}) flat panel photobioreactor (Fig B, Supplementary Materials). The photobioreactor is described elsewhere (Fig A, Supplementary Materials) (Zeriouh et al. 2019). The high PBR volume/flow cell volume ratio allows one to compare different recirculation flows without affecting the culture (Teodósio et al. 2012). The connection pipes were sufficiently long and narrow to avoid cell adhesion inside them, as recommended by Ozkan (2012). In the PBR, perfect mixing was imposed (Teodósio et al. 2012).

For both the validation tests and the simulations, two different culture flow rates were considered: the maximum allowed by the flow cell (3.5 mL·min^{-1}) and another flow rate more than 10-times lower (0.3 mL·min^{-1}). Each recirculation experiment lasted approximately 2 hours, with residence times throughout the flow system close to 1 and 12 min for the maximum and minimum flow rates, respectively. The experiments were repeated 5 times to obtain representative results.

After extracting the coupons from the flow cell, the amount of adhered cells was determined using the technique reported by Zeriouh et al. (2017). Briefly, after a gentle washing with sea water, the coupons were transferred to a 48-well 3D printed plate adapted especially for them. The Chlorophyll *a* (Chl*a*) fluorescence intensity was then measured (Ex. 480 nm; Em. 685 nm) in a plate reader (SynergyMx®, BioTek Instruments Inc., Vermont, USA) at 21 different positions on the coupon (see Figure C in the Supplementary Materials section). From these readings, it was possible to obtain a microalgal adhesion map by interpolation.

2.4.   Adhesion model

As recommended by Boks et al. (2008), the cell-surface interaction forces can be obtained by deriving the expressions of the surface free energy from the XDLVO model with respect to the distance to the surface (*d*). In this work, the XDLVO model formulation developed by Ozkan and Berberoglu for microalgae has been used (Ozkan & Berberoglu 2013).

The Lifshitz-Van der Waals force for particle-surface interactions was calculated as:

$$F_{LW}(d) = \frac{2 \cdot A \cdot a^3}{3 \cdot d^2 \cdot (2 \cdot a + d)^2} \tag{1}$$

8

where a is the radius of the microalgae cell (m), d is the distance between the cell surface

and the wall (m), and A is Hamaker's constant ($A = 1.57$ N·m (van Oss 2008)).

The electrostatic component of the force balance is given by:

$$F_{EL}(d) = \frac{\pi \cdot a \cdot \varepsilon \cdot \kappa \cdot (\exp(-\kappa \cdot d) \cdot \psi_s \cdot \psi_m + \exp(-\kappa \cdot d) \cdot \psi_m^2)}{\sinh(\kappa \cdot d)} \tag{2}$$

where ε is the electrical permittivity of the medium (F·m^{-1}), and ψ_s and ψ_m are surface

potentials of the surface and the microalgae, respectively, (V). These magnitudes were

calculated as described in Zeriouh et al. (2017).

$$\psi_{m\,or\,s} = \varsigma_{m\,or\,s} \cdot \left(1 + \frac{\upsilon}{a}\right) \cdot \exp(\kappa \cdot \upsilon) \tag{3}$$

where ς_m and ς_s are the zeta potentials of the microalgae and the surface, respectively, υ

denotes the thickness of the hydration layer attached to the microalgae (m), and κ^{-1} is the

thickness of the double electrical layer (Zeriouh et al. 2017).

The Lewis acid-base force is obtained from the acid-base energy:

$$F_{AB}(d) = -2 \cdot \pi \cdot a \cdot \Delta G_{adh}^{AB} \cdot \exp\left(\frac{d - d_0}{\lambda}\right) \tag{4}$$

where λ is the gyration radius of the water molecules in the culture medium (m) and

$\Delta G^{AB}{}_{adh}$ is the acid-base component of the adhesion surface free energy (J m^{-2}) (Zeriouh,

et al. 2017).

$$F_{XDLVO}(d) = F_{LW}(d) + F_{EL}(d) + F_{AB}(d) \tag{5}$$

The drag force (F_{drag}) is caused by friction between the particle and the fluid. This

force is proportional to the viscosity of the fluid (μ_f; N·s·m^{-2}), the relative velocity of

the particle with respect to the fluid ($U_f - U_p$; m·s^{-1}), and the area of the particle

perpendicular to the flow. For small quasi-spherical particles, Stokes' Law can be used (O'Neill 1968).

$$F_{drag} = 6 \cdot f \cdot \pi \cdot a \cdot \mu_f \cdot (U_f - U_p) \tag{6}$$

where f is a friction factor; in our case it was 1.7009 (O'Neill 1968).

The lift force is perpendicular to the drag force. This force acts in the opposite direction to the adhesion, which moves the particle away from the surface. For small spherical particles, the lift force is calculated, according to Saffman (Saffman 1965), as:

$$F_{Lift} = 81.2 \cdot \mu_f \cdot a^2 \cdot \left(\frac{\dot{\gamma} \cdot \rho_f}{\mu_f}\right)^{\frac{1}{2}} \cdot (U_f - U_p) \tag{7}$$

where ρ_f is the density of the fluid (kg·m^{-3}) and $\dot{\gamma}$ is the shear rate (s^{-1}).

The buoyant force is the force caused by submerging a body in a fluid. This is proportional to the volume displaced by the body itself. Thus, the net weight of the particle in the fluid will be the difference between the buoyant force and its own weight.

$$F_w = g \cdot \frac{(\rho_p - \rho_f)}{\rho_p} \cdot m_p \tag{8}$$

where g is the acceleration of gravity (m·s^{-2}), ρ_p is the density of the particle (kg·m^{-3}) and m_p is the mass of the particle (kg).

The net force acting on a cell close to a solid surface is therefore:

$$\Sigma F = F_{drag} + F_w + F_{Lift} + F_{XDLVO} \tag{9}$$

The value of the parameters involved in equations 1 to 8 needed to calculate ΣF in eq (9) are collated in Table 1 and Table 2. The surface values correspond to the cleaned PMMA coupons.

2.5. Adhesion criteria

Particles within a fluid circulating near a wall are subjected to forces that may adhere them to, or move them away from, the surface (Figure E, Supplementary Materials). The adhesion criterion used in this work is based on classical mechanics, where forces and moment balances are used (Henry 2018). Microalgal wall adhesion in a photobioreactor occurs if a static equilibrium is achieved. Therefore, an eventual break-up of that equilibrium would lead to cell detachment. As these are very short-range forces, they will only be relevant at a distance of a few nanometres away from the surface (Bos et al. 1999).

There are three processes that can break the static equilibrium: detachment, slip, and rotation. The detachment and slip criteria are derived from force balances, while the rotation criteria is derived from a balance of moments. According to Henry (2018), the three criteria (R) are established as follows:

$$R_{Detachment} = \frac{F_{Lift}}{F_w + F_{XDLVO}} \tag{10}$$

$$R_{Slip} = \frac{F_{drag}}{k_s \cdot (F_{Lift} + F_{XDLVO} + F_w)} \tag{11}$$

$$R_{Rotation} = \frac{a \cdot F_{drag} + r_c \cdot F_{Lift}}{r_c \cdot (F_{XDLVO} + F_w)} \tag{12}$$

where k_s is a slip coefficient (~0.3); and r_c is the contact radius obtained from Hertz's theory (Yap et al. 2016). A cell will move from the position where it is attached when one

of the three criteria (R) above is greater than unity. Once the net adhesion force experienced by the particle (F) has been determined, r_c can be calculated from Equations 13, 14, and 15.

$$F = \frac{4}{3} \cdot E^* \cdot a^{1/2} \cdot \delta^{3/2} \tag{13}$$

Where:

$$\frac{1}{E^*} = \frac{1 - v_1^2}{E_1} + \frac{1 - v_2^2}{E_2} \tag{14}$$

E_1 and E_2 (Pa) represent the Young's modulus of the cell and the surface, respectively (see Table 1); δ (m) is the deformation of the cell radius in contact with a surface; and v_1 and v_2 are the Poisson's radii for the cell (1) and the PBR material (2), respectively (Table 1). Finally, the contact radius is obtained as follows:

$$r_c = \sqrt{a \cdot \delta} \tag{15}$$

2.6. CFD Simulation

This was performed for 3D geometry in transient mode using the ANSYS Fluent® 2020R1 commercial software (Ansys Inc., Pennsylvania, USA). The calculations were carried out using a HP Z840 Workstation with 2 Intel Xeon® E5-2670v3 processors of 12 cores each, a total of 24 cores used in parallel, and 128 GB of RAM.

2.6.1. Geometry and meshing

The geometry of the flow cell was represented using the ANSYS DesignModeler® module (Figure 1b). Possible minor design imperfections or surface roughness in the flow channel were not considered in the simulations. The surface of the flow cell in contact with the culture is considered smooth (having a mean surface roughness below 0.6 μm). The mesh was made with ANSYS Meshing® (Fluent solver preference module). Mesh

refining was performed on the coupon walls in order to have two mesh elements in the diffusion layer (Dąbroś & Van De Ven 1982). For this, inflation layers with an initial cell size of 2 μm were used (Figure 2). A mesh independence analysis was performed using 1, 2, and $5.4 \cdot 10^6$ cells, and minor differences in fluid velocity profiles and wall shear stress were obtained for meshes with more than $2 \cdot 10^6$ cells (Figures H-K in Supplementary Materials). Despite the small variation observed, the most refined mesh was used in the simulations to increase the numerical accuracy of the particle deposition positions on the coupons. The polyhedric mesh of $5.4 \cdot 10^6$ cells had a minimum orthogonal quality of 0.7 (acceptable value ≥ 0.1; Halder et al., 2014). In Figure 2, the different areas of the mesh can be seen.

2.6.2. Fluid flow

The isothermal turbulent flow of the fluid was solved using a Eulerian approach. The continuity and Navier-Stokes equations were solved using the finite volume method. As the volumetric fraction of the particles in the culture was near 0.06% (much lower than 5%), the suspension properties were assumed to be equal to those of sea water (Adamczyk et al. 2000): a density of 1023 kg·m^{-3} and a viscosity of 0.00103 kg·m^{-1}·s^{-1}. A constant flat velocity profile was assumed at the inlet, as suggested by Dimartino et al. (2014).

The outlet was modelled as a pressure outlet ($P = 1$ atm). The force of gravity was included in the z axis, in the negative direction. Although the flow is laminar, the simulation was performed in turbulent mode, using the SST k-ω model with low Reynolds number corrections. Thus, it was possible to capture any flow disturbance that might be generated at the inlet, outlet or coupon extraction slits (Moreira et al. 2015). This strategy has been shown to lead to accurate simulations, both in free stream and wall-bounded flows (Teodósio et al. 2012). Furthermore, Stone et al. (2019) demonstrated that laminar flow can be correctly described by turbulent models such as k-ε, k-ω and SST k-ω.

Pressure-velocity coupling was achieved using the SIMPLE algorithm. The convective

terms were discretized with the QUICK scheme. The PISO formulation was used to solve

the pressure-velocity coupling (Teodósio et al. 2012). The second-order upwind spatial

discretization scheme was used to calculate the turbulent kinetic energy (k) and the

specific rate of energy dissipation (ω). The non-slip boundary condition for the liquid

was assumed in the walls (Adamczyk et al. 2000). Time step sizes of 0.003 and 0.001 s

were observed to be small enough to achieve high numerical accuracy for the lowest and

highest liquid flow rates, respectively. These values also ensured the accurate description

of the contact and transport times (Dąbroś & Van De Ven 1982; Busscher & Van Der

Mei 2006). Residuals for all the variables were fixed at 10^{-5} for each flow step. For both

flow rates, the total simulation times were 200 seconds after flow stabilization.

2.6.3. Particle model

The cells have been modelled as spherical particles with the properties of *N.*

gaditana, (4 μm in diameter and 1200 kg·m^{-3} in density (Zeriouh et al. 2017)). The

injection of the particles was carried out by distributing them homogeneously at the flow

cell inlet; 90,000 particles were injected in each simulation.

The particle trajectory modelling was carried out using the DPM module included in

ANSYS Fluent®. Since the particle volume fraction (α_p) was $6\cdot10^{-4}$, 2-way coupling was

used (Greifzu et al. 2016). This model is based on a Lagrangian approach, which consists

of individual monitoring of each particle to determine its trajectory without considering

the interaction between them (Zhao & Zhao 2020). The Discrete Random Walk Model

(DRWM) was used to include the effects of turbulent fluctuations on particle trajectories,

as this has been demonstrated to accurately represent the transport of particles to surfaces

(Yan et al. 2020). As Fluent's DPM model does not include particle-wall interactions

14

1
2
3
4
5
6
7
8
9
10
11
12
13
14
15
16
17
18
19
20
21
22
23
24
25
26
27
28
29
30
31
32
33
34
35
36
37
38
39
40
41
42
43
44
45
46
47
48
49
50
51
52
53
54
55
56
57
58
59
60

(Zhao & Ambrose 2019), the previously described XDVLO-based adhesion model was included in a UDF (see Figures G in Supplementary Materials). This UDF performed the balance of forces expressed in equation 8 to determine the net force acting on each particle.

The boundary condition for the coupon walls was "perfect sink" (Elimelech 1994). Finally, the adhesion criteria were introduced in the simulation with a UDF (see Figure F in Supplementary Materials). When a particle got close enough to a wall, the UDF was executed and, after reading the data from the other UDFs, the ratios of equations 10, 11 and 12 were calculated. If the three conditions were lower than 1, it was established that the particle would adhere. In that case, the UDF aborted the tracking of the adhered particle and recorded the particle's position data in a file. Otherwise, its trajectory continued to be obtained (Figure F in Supplementary Materials).

2.6.4. Statistical analysis

A multifactor ANOVA was performed to determine the effect of the following factors and their interactions on the adhesion data measured: position of the coupon in the flow cell (3 positions), measuring point on the coupon (21 points), culture flow rate (2 flow rates) and replicate (5 replicates). Statistically significant differences in the mean response between factors were fixed at a 5.0% significance level threshold ($p < 0.05$). The method used to discriminate between the means at the 95.0% confidence level was Fisher's least significant difference (LSD) procedure. Statistical data analyses were performed using the Statgraphics Centurion XIX (StatPoint, Herndon, VA, USA).

3. Results

3.1. Liquid velocity

For the validation tests and the simulations, two different liquid flow rates were considered: the maximum recommended by the flow cell maker (3.5 mL·min^{-1}) and a very low flow (0.3 mL·min^{-1}). The Reynolds number (Re) corresponding to each flow was calculated in accordance with Dimartino et al. (2015). At both flow rates and throughout the cell, the fluid would circulate in laminar flow. Thus, in the inlet and outlet tubes, the Re values were around 50 for the maximum flow and 5 for the minimum flow used. However, in the channel, the Re values were 20 for the maximum flow and 2 for the lesser flow.

In the simulations, a turbulence model was considered to capture the possible turbulences generated in the inlet/outlet areas or near the coupon extraction slits. The model chosen was the SST k-ω turbulent RANS model. This model was chosen because it solves the Navier-Stokes equation and the kinetic energy balance (k) within the viscous sublayer, without the need for empirical wall functions, as required by the k-ε models. Notwithstanding, a comparative simulation was carried out under the most unfavourable conditions (the lower flow rate tested, $Re = 2$) using the turbulence model and the laminar model. Figure 3 represents the velocity profiles obtained with both models in the centre of the flow cell, along transverse lines (x = constant, z = 200 μm). One can observe that both models give identical results, irrespective of the coupon considered. Therefore, the use of the k-ω model is justified for solving possible disturbances in the flow.

Likewise, one can see that the flow is parabolic and symmetrical with respect to the centre of the coupon in the first and third coupons (the entry and exit coupons) (Figures 3a and 3c). However, in the central coupon, the velocity profile in the y direction is totally

16

flat except in the area close to the walls. When the dimensionless velocity (U_f / U_0) is plotted against the x dimension, following a line ($y = 0$; $z = 200$ μm) through the centre of the flow cell (Figure 3d), one can observe that the velocity is not constant in the inlet and outlet zones. There was a significant increase in the velocity in these zones and some decrease in between the coupons (caused by the coupon extraction slits). Only over the central coupon was a steady velocity observed along all its length. The behaviour was almost identical for both flows since they are laminar flows.

Figures 4 and 5 show the velocity magnitude in the flow cell for both flow rates tested. As can be observed, the difference between the values is proportional to the ratio between the flows.

As observed from the velocity vectors and fluid trajectories, the fluid passes parallel to the coupons at both flow rates, which confirms the laminar flow (Figures 4b, c and 5b, c). At maximum flow, the flow is more disordered at the outlet but does not affect the rest of the flow cell. The maximum velocities are reached in the inlet and outlet channels at both flow rates, with velocities of 0.1 m·s^{-1} and 0.01 m·s^{-1}, respectively. One can further appreciate that the slits for facilitating coupon extraction disturbed the flow.

3.2.   Shear stress

Shear stress (σ_w) on solid surfaces has been used frequently to quantify and explain cell adhesion (Pereira et al. 2002; Dimartino et al. 2014). At the highest flow rate tested (3.5 mL·min^{-1}), the mean values were 0.229, 0.176 and 0.234 Pa for the inlet, centre and outlet coupons, respectively. In the case of the lower flow rate (0.3 mL·min^{-1}), the behaviour was the same, although the values obtained were an order of magnitude lower, corresponding to a σ_w of 0.021, 0.016 and 0.021 Pa for the inlet, centre and outlet coupons, respectively. For each flow rate, although the values calculated are similar for the 3 coupons, a significant difference can be seen between the central coupon and those of the

17

1
2
3
4
5
6
7
8
9
10
11
12
13
14
15
16
17
18
19
20
21
22
23
24
25
26
27
28
29
30
31
32
33
34
35
36
37
38
39
40
41
42
43
44
45
46
47
48
49
50
51
52
53
54
55
56
57
58
59
60

extremes affected by the entry and exit effects (Figures 4 and 5) presenting the highest σ_w

values (See Figure 6). The differences between the inlet-outlet coupons and the central

coupon are greater ($\sim$ 25%) at the higher flow rate.

Figure 6 shows the spatial shear stress fields on the inlet (top) and outlet (bottom)

coupons. The distribution pattern was similar for both flow rates. The areas with the

highest σ_w values were found in the entry and exit of the flow cell, these areas being

somewhat wider at the higher flow rate. In addition, the maximum values of σ_w were 0.55,

0.32 and 0.77 Pa for the inlet, centre, and outlet coupons at the 3.5 mL·min^{-1} flow rate,

and 0.057, 0.031 and 0.061 Pa at the 0.3 mL·min^{-1} flow rate. Areas of greater shear stress

are also seen at the lower flow rate on the sides of the inlet and outlet coupons. In contrast,

as might be expected from the velocity profiles discussed in the previous section, the σ_w

distribution on the central coupon is relatively homogeneous over almost the entire

surface.

3.3.   Hydrodynamic forces

As explained above, the equations for determining the F_{drag} and F_{lift} by CFD were

implemented using UDFs.

Figures 7 show the drag and lift force fields inside the flow cell on a plane located at

the distance of "a" (i.e., 2 μm) from the surface of the coupons for the two flow rates

tested. At the maximum flow, the maximum value of the lift force was 9·10^{-13} N, while

at the minimum flow, it was around 3·10^{-14} N. This force is, therefore, an order of

magnitude lower than the drag force (9·10^{-13} N and 9·10^{-12} N for the minimum and

maximum flows, respectively). Both F_{drag} and F_{lift} showed a similar distribution pattern

for the two flow rates, the values being an order of magnitude greater for the maximum

18

flow. In Figures 7c and 7d, one can observe that the lift force, as with the drag force, is influenced by the local velocity of the liquid. Thus, their distributions were very similar.

3.4. Cell-surface force

The force resulting from cell-surface interactions, calculated according to the XDLVO model (Equations 1-5) at the minimum distance (d_0), would be that of repulsion for clean PMMA coupons due to the so-called double-repulsion layer (Figure D in the Supplementary Materials). It is to be expected that if fouling is eventually generated, the surface properties have to evolve to a situation in which the force curve falls within the irreversible adhesion zone (Bos et al. 1999). Thus, for the simulations, it was assumed that the properties of the PMMA coupons are those corresponding to the latter situation and not to their initial state (Blue line in Figure D, Supplementary Materials) as it was intended to qualitatively predict the distribution of fouling on the solid surfaces.

Since the XDLVO model forces do not depend on flow, they are constant throughout the cell. For the minimum distance (d_0), a resultant force value of $4 \cdot 10^{-8}$ N was obtained; this is the one used in the UDF that applies the adhesion criteria (Figure G in the Supplementary Materials).

3.5. Adhesion assays

Table 3 displays the analysis of variance (multifactor ANOVA) decomposing the variability in the adhesion measurements into several components: (i) a component attributable to the main effect of each factor considered in section 2.6.4.; (ii) another one attributable to the interactions between factors. Except for the factors *replicate* and *flow rate*, the remaining factors had a statistically significant effect on cell adhesion at the 95% confidence level (*p*-value < 0.05) (Table 3). The factor *coupon* was responsible for most of the variance observed (*F*-ratio = 72.29), followed by the factor *measurement position*

on the coupon that showed an influence more than 10 times lower (*F*-ratio=6.71). Only four interactions between factors were relevant (see Table 3), the interaction *coupon-culture flow* being the most statistically significant. The Multiple Range Test from ANOVA allowed us to perform a multiple comparison procedure to determine which means are significantly different from which others. Seven homogenous groups were identified for the 21 different measuring points on the coupons (Table 3).

Regarding the simulations, a total of 90,000 particles were injected homogenously through the flow cell inlet over a perpendicular plane. The injection was then stopped to allow the particles to either attach or escape from the flow cell. The simulation time was 200 s. This was long enough for around 30,000 particles to adhere. For a more detailed description of the adhesion, each coupon was divided into 6 portions (Figure 8). At both flow rates (0.3 mL·min^{-1} and 3.5 mL·min^{-1}), the greatest adhesion to the inlet coupon (Fig 8 a, c) was predicted to occur in the vicinity of the greatest wall shear stress (See Figures 8a and b). The experimental adhesion assays for *N. gaditana,* the results of which are shown in Figures 8 b, d, also satisfactorily support the simulation estimations. However, it can be seen that the zone with adhered cells extended further (especially at 0.3 mL·min^{-1}).

After the inlet coupon, at both flows, the central path, which contained a lower percentage of adhered cells in the simulations (Figs. 10 a, c), was also roughly reproduced in the experimental observations (Figs. 10 b, d). On both sides of this central path, there was generally an equitable distribution of adhered cells. On this central coupon, the main difference between the simulation and the validation was that in the latter, the adhesion was distributed in the four corners of the coupon. For the outlet coupons, besides the central path, it was evident that the cells started adhering to both sides of the first half.

4. Discussion

4.1.   Liquid flow

To evaluate flow behaviour at the microscale, it is advisable to perform calculations that can capture flow perturbations with sufficient precision. Although the average magnitudes are clearly laminar, small areas near constrictions (slits, etc.) could alter the flow, resulting in turbulent properties in small volumes of the system.

As can be observed in Figures 5, even in the most unfavourable case (a flow rate of 0.3 mL·min^{-1}), the chosen turbulence model (SST k-ω with a low Reynolds correction) produced liquid velocity results identical to the laminar model. These results are in agreement with the observations of other authors (Stone et al. 2019).

Although the width-to-height ratio in the flow cell is greater than five to prevent side-wall effects, the inlet and outlet pipes were positioned perpendicular to the flow. This generates clear flow deformations (See Figs. 4 and 5) that cannot be compensated for by the triangular sections in the flow cell. This causes the liquid passing over the central area of the inlet/outlet coupons to circulate at higher speeds than at the periphery (in the direction of the cell width). Even though significant perturbations in flow have been documented in similar flow cells (Bos et al. 1999), the flow cell manufacturer continues to commercialise this device. Hence, these results were expected, since it is well documented that significant variations in liquid velocity develop in the entry zone of these flow systems (Teodósio et al. 2011). Thus, a flat velocity profile, which is desired in these flow devices (Bakker et al. 2003; Dimartino et al. 2014), is only observed for the central coupon (Figure 3b).

As discussed above, it is known that areas exist in the flow cells which are affected by flow perturbations as the liquid enters and exits (Bakker et al. 2003; Busscher & Van

Der Mei 2006). This becomes a critical issue when such perturbations provoke the liquid

to exhibit a different flow regime over one or more coupons. If ignored, this may lead to

invalid cell adhesion results when comparing coupons made of different materials

(Moreira et al. 2013; Zeriouh et al. 2019). The ideal flow cell should allow a fully

developed flow before arriving at the entrance to the first coupon (Busscher & Van Der

Mei 2006). Our simulations clearly suggested that typical calculations on the channel

entry length cannot be applied to all geometries, as equations are generally developed for

uniform inflow between parallel plates. This does not occur in the flow cell evaluated in

this work. Consequently, calculations of the hydrodynamic inlet length (*Le*), (i.e., the

distance from the inlet at which the flow is fully developed, according to Han, 1960)

provided dramatically low *Le* values (0.21 and 0.018 mm for the maximum and minimum

flow rates, respectively).

However, our results from Figure 3d provide compelling evidence that velocity can

be considered constant on very small portions of the coupons located at the inlet and

outlet, and on a large proportion of the central coupon surface. This discrepancy is caused

by Han's equation, since its use is limited to systems in which the fluid enters aligned

with the largest dimension of the cell and not perpendicular to it, as was the case in this

work.

Shear stress values have been considered important in particle deposition, biofilm

formation and cell detachment (Ozkan & Berberoglu 2013; Tang et al. 2013; Yan et al.

2020). Up to a certain limit, shear stress transports cells to the surfaces and, when cell

adhesion has occurred, may provoke detachment of the cells (Roosjen et al. 2005). For a

geometry such as the one used, the theoretical shear stress for a Newtonian fluid can be

calculated from the following equation (Dimartino et al. 2014):

22

$$\tau_w = \frac{6 \cdot Q \cdot \mu}{h_0^2 \cdot w_0} \tag{17}$$

where Q is the flow rate (in this case 3.5 or 0.3 mL·min^{-1}), μ is the viscosity of the liquid (0.00103 Pa·s for seawater), and h_0 and w_0 are the thickness and width of the cell channel (0.4 mm and 12.9 mm, respectively). As expected, the highest σ_w values were obtained for the highest flow, the difference being proportional to the ratio between flows. The results obtained for each flow are of the order of 0.25 and 0.0215 Pa. These average values are very similar to those obtained in the simulation (Fig. 6), despite not having a perfectly homogeneous flow in the flow cell.

4.2.   Forces

The properties of the surfaces in contact with a microbial suspension change over time due to the formation of conditioning layers prior to cell adhesion (Bos et al. 1999; Pereira et al. 2002; Halder et al. 2013).

This causes the values of the energies calculated according to the XDLVO model to also change over time, and thus those of the cell-surface interaction forces (Zeriouh et al. 2017). The timescale for surface conditioning and adhesion is in the order of hours at a minimum (Halder et al. 2013), whereas CFD flow simulations cannot be extended beyond a few minutes. It is therefore impossible to simulate the entire cell adhesion process using this technique. Moreover, in real assays, up to 10^9 cells per hour would pass through the flow cell, whereas the DPM-CFD simulations typically handle much lower numbers of particles (e.g., $\square 10^5$ particles in 1 min of simulation). However, it is possible to use CFD simulations to predict the flow system locations where cell adhesion is most likely.

The drag force is usually the strongest of the hydrodynamic forces. With maximum values of about 9 pN, it might in some cases prevent cell adhesion and even detach cells adhered to the coupons (Boks et al. 2008). Nonetheless, due to the high net interaction

23

force value corresponding to the XDLVO model in the conditioned PMMA coupons ($40 \cdot 10^4$ pN), it was not enough to prevent adhesion. The lift force is generally considered negligible when it comes to preventing the development of biofouling, as it is much weaker than the adhesion, drag force or shear forces. On the other hand, drag and shear forces might cause particle/cell detachment (Sharma et al. 1992; Busscher & Van Der Mei 2006). Although the lift force is added to the drag force to avoid cell-surface attachment (Zeriouh et al. 2017), in this case, the magnitude calculated would be a maximum of 9.9 pN, a value that would not be enough to prevent cell adhesion. The lift force, however, helps to transport the cells away from the surface once the interaction between the cells and surface is broken (Boks et al. 2008).

4.3.   Cell adhesion

Flow cells have traditionally been used to study cell adhesion on solid surfaces. Homogeneous particle deposition is usually expected when the flow velocity is constant in a flow device (Paul et al. 2012). It should be noted that in the validation tests, only the central coupon showed an adhesion pattern close to homogeneity. The distribution of cells on the coupons showed a strong statistical difference (Table 3) and that detail should be considered when performing adhesion assays for comparing different materials. In this sense, if a longer flow cell with a greater number of coupons were used, it would most likely be possible to evaluate the adhesion on serial coupons subjected to the same hydrodynamic conditions under a fully developed flow. CFD simulations help in characterizing the flow in such devices and in identifying the coupons that are not subjected to homogeneous flow (Zeriouh et al. 2019). However, it has been reported that the cell distribution is not usually homogeneous on the surfaces of the coupons in flow cells (Pereira et al. 2002). The statistical analysis in this study also confirmed that the cells do not distribute homogeneously on the same coupon (Table 3). The distribution of

24

the 21 different measuring points into 7 homogeneous groups indicate that the resolution

of the measuring method was high enough to obtain highly-defined adhesion maps.

σ_w has been frequently used to describe cell adhesion and biofilm structure on surfaces

under flow (Busscher & Van Der Mei 2006; Ozkan & Berberoglu 2013; Dimartino et al.

2014). However, several authors have questioned the exclusive use of shear stress to

predict cell adhesion. For instance, this parameter does not consider the size and shape of

the microorganisms, the surface characteristics of the cells, the surfaces, or the flow field

away from the wall (Dimartino et al. 2014). Shear stress cannot cause detachment but

rather causes sliding until the cell encounters less favourable conditions on the surface

and detaches itself (Busscher & Van Der Mei 2006). It is therefore important to determine

its value on each coupon in a flow cell. According to our simulations, the shear stress

profiles were symmetrical (Figure 6), so if the adhesion criterion implemented had been

based on shear stress, zones with heterogeneous biofouling distribution should not have

been observed. Both the actual flow cell and the simulated cell showed heterogeneous

adhesion on the coupons' surfaces.

The values calculated for the adhesion force (according to the XDLVO model) were

orders of magnitude higher than the lift and drag forces. These results agreed with those

obtained by Ozkan and Berberoglu in a similar flow cell (Ozkan & Berberoglu 2013).

Hence, under these conditions, adhesion would occur when the particle gets close enough

to the surface. In addition, considering the low flow rates and shear stresses generated,

the deadhesion phenomenon would be unlikely to occur (Ozkan 2012). The values of the

forces that could cause deadhesion (lift and drag) are much lower than 10^{-10}-10^{-11} N,

which are the reference values for microorganism detachment from solid surfaces (Rutter

& Vincent 2018), and clearly below the XDLVO adhesion force value.

The magnitudes that directly depend on flow rate (shear stress, drag and lift forces) have been demonstrated to have not a significant influence on cell adhesion. This was expected since, despite existing a one-order of magnitude difference between the two culture flow rates assayed, there were no observed significant differences in the distribution of the mentioned variables (Figures 6 and 7). The statistical analysis also confirmed the absence of statistical influence of Q on cell distribution on the coupons (Table 3). Although the different coupons and positions on the coupon (AC, BC and ABC combinations in Table 3) showed statistical different cell adhesion at different flow rates.

The DPM-CFD model in this work has been validated with experimental measurements of *N. gaditana* adhesion (Fig. 8). As initial cell adhesion takes place once the solid surface has been conditioned, it is practical to use the surface properties corresponding to the conditioned conditions for the CFD simulations. Despite some differences between the experimental and simulated values, it was shown that the CFD results qualitatively identified areas that had a higher probability of developing biofouling. In CFD simulations, it is not possible to calculate the entire period necessary for the complete development of the biofilm (from hours to days). Thus, the greatest difficulty in validating the simulations with the experimental results is that measurements under experimental conditions can only be taken at a given time. On the other hand, the adhesion measured in the actual flow cell is the result of a gradual conditioning of the coupon surface. Furthermore, the timescales and the number of simulated particles and cells are, by necessity, different between the real and simulated systems. Consequently, it is difficult to determine whether the profiles of the same relative moment are being compared or not; nevertheless, our validation results are compatible with the adhesion pattern obtained in the simulation. From that moment on, the microalgal cells had to adhere to different locations in the validation flow device since an adhered cell would

26

produce cell-to-cell repulsion. This phenomenon was not included in our model because those particles that adhere to the surface disappear from the simulation (the perfect sink boundary condition). In longer validation assays, an expansion of the adhesion zones would be observed. On the other hand, adhered cells may cause flux perturbation resulting in greater heterogeneity in the adhesion pattern (Dimartino et al. 2014). This cannot be modelled with Lagrangian particle tracking, so they would not affect the flow. It has been shown that attached particles larger than 1 μm disturb the flow around themselves, making it difficult for other particles to adhere to the same area. This effect can be extended over areas up to 25-times the cell size (Dąbroś & Van De Ven 1982; Adamczyk et al. 2000). This cell-flow interaction could be another source of the disparity observed between the simulations and the validation results. In this regard, several authors have observed a heterogeneous cell distribution in the early stages of biofouling formation (Chang et al. 2020). When the biofilm is large enough (macroscopic), the flow perturbations are more relevant, even affecting the laminar flow regime.

5. Conclusions

To the best of our knowledge, this is the first CFD model that integrates flow properties, particle tracking and XDVLO force balance. The model was validated with microalgae suspensions. Although it has been claimed that flow cells do not properly mimic real systems (Bos et al. 1999), they have proven useful as validation systems for CFD. With the methodology proposed in this work, biofilm onset in different flow systems could be qualitatively predicted. This is of critical importance in various biotechnological fields, such as in biofouling avoidance in bioreactors. Once cell adhesion starts, it is practically impossible to avoid biofouling developing – being able to identify

those areas most prone to initial cell adhesion would allow us to optimize the design of

the culture systems to prevent biofouling from beginning in the first place.

Acknowledgements

Bibliography

Adamczyk Z, Warszyński P, Szyk-Warszyńska L, Weroński PX. 2000. Role of convection in particle deposition at solid surfaces. Colloids Surfaces A Physicochem Eng Asp. 165(1–3):157–187.

Ansys-Fluent. 2003. Fluent 6.1 User's guide.

Azeredo J, Azevedo NF, Briandet R, Cerca N, Coenye T, Rita Costa A, Desvaux M, Di Bonaventura G, Hébraud M, Jaglic Z, et al. 2017. Critical review on biofilm methods. Crit Rev Microbiol. 43(3):313–351.

Bakker DP, Van der Plaats A, Verkerke GJ, Busscher HJ, Van der Mei HC. 2003. Comparison of Velocity Profiles for Different Flow Chamber Designs Used in Studies of Microbial Adhesion to Surfaces. Appl Environ Microbiol. 69(10):6280–6287.

Barker BJ. 2010. Simulation of Coal Ash Deposition on Modern Turbine Nozzle Guide Vanes. [place unknown]: The Ohio State University.

Becker W. 2007. Microalgae in Human and Animal Nutrition. In: Handb Microalgal Cult. Oxford, UK: Blackwell Publishing Ltd; p. 312–351.

Boks NP, Norde W, Van Der Mei HC, Busscher HJ. 2008. Forces involved in bacterial adhesion to hydrophilic and hydrophobic surfaces. Microbioloy. 154:3122–3133.

Bos R, Van Der Mei HC, Busscher HJ. 1999. Physico-chemistry of initial microbial adhesive interactions - Its mechanisms and methods for study. FEMS Microbiol Rev. 23(2):179–230.

Busscher HJ, Van Der Mei HC. 2006. Microbial adhesion in flow displacement systems. Clin Microbiol Rev. 19(1):127–141.

Chisti Y. 2010. Fuels from microalgae. Biofuels. 1(2):233–235.

Christaki E, Florou-Paneri P, Bonos E. 2011. Microalgae: A novel ingredient in nutrition. Int J Food Sci Nutr. 62(8):794–799.

Coons JE, Kalb DM, Dale T, Marrone BL. 2014. Getting to low-cost algal biofuels: A monograph on conventional and cutting-edge harvesting and extraction technologies. Algal Res. 6(PB):250–270.

Dąbroś T, Van De Ven TGM. 1982. Kinetics of coating by colloidal particles. J Colloid Interface Sci. 89(1):232–244.

Dimartino S, Mather A V., Alestra T, Nawada S, Haber M. 2014. Experimental and computational analysis of a novel flow channel to assess the adhesion strength of sessile marine organisms. Interface Focus. 5(1):1–12.

Elimelech M. 1994. Particle deposition on ideal collectors from dilute flowing suspensions: Mathematical formulation, numerical solution, and simulations. Sep Technol. 4(4):186–212.

Ellison W, Balana A, Delbos G, Lamkaouchi K, Eymard L, Guillou C, Prigent C. 1998. New permittivity measurements of seawater. Radio Sci. 33(3):639–648.

Greifzu F, Kratzsch C, Forgber T, Lindner F, Schwarze R. 2016. Assessment of particle-tracking models for dispersed particle-laden flows implemented in OpenFOAM and ANSYS FLUENT. Eng Appl Comput Fluid Mech. 10(1):30–43.

Halder P, Nasabi M, Jayasuriya N, Shimeta J, Deighton M, Bhattacharya S, Mitchell A, Bhuiyan MA. 2014. An assessment of the dynamic stability of microorganisms on patterned surfaces in relation to biofouling control. Biofouling. 30(6):695–707.

Halder P, Nasabi M, Lopez FJT, Jayasuriya N, Bhattacharya S, Deighton M, Mitchell A, Bhuiyan MA. 2013. A novel approach to determine the efficacy of patterned surfaces for biofouling control in relation to its microfluidic environment. Biofouling. 29(6):697–713.

Henry C. 2018. Particle resuspension from complex surfaces: current knowledge and limitations. arXiv arXiv:180206448.

Johnston MD, Jones M V. 1995. Disinfection tests with intact biofilms: combined use of the Modified Robbins Device with impedance detection. J Microbiol Methods. 21(1):15–26.

Kallio GA, Reeks MW. 1989. A numerical simulation of particle deposition in turbulent boundary layers. Int J Multiph Flow. 15(3):433–446.

Kang C, Li Q, Li M, Teng S. 2020. Deposition of solid particles exposed to the suction of dual pumps in the tank of a pumping station. Powder Technol. 361:727–738.

Koyande AK, Chew KW, Rambabu K, Tao Y, Chu DT, Show PL. 2019. Microalgae: A potential alternative to health supplementation for humans. Food Sci Hum Wellness. 8(1):16–24.

López-Rosales L, Gallardo-Rodríguez JJ, Sánchez-Mirón A, Cerón-García MDC, Belarbi EH, García-Camacho F, Molina-Grima E. 2014. Simultaneous effect of temperature and irradiance on growth and okadaic acid production from the marine dinoflagellate *Prorocentrum belizeanum*. Toxins (Basel). 6(1):229–253.

McLaughlin JB. 1989. Aerosol particle deposition in numerically simulated channel flow. Phys Fluids A. 1(7):1211–1224.

Moreira JMR, Araújo JDP, Miranda JM, Simões M, Melo LF, Mergulhão FJ. 2014. The effects of surface properties on *Escherichia coli* adhesion are modulated by shear stress. Colloids Surfaces B Biointerfaces. 123:1–7.

Moreira JMR, Ponmozhi J, Campos JBLM, Miranda JM, Mergulhão FJ. 2015. Micro- and macro-flow systems to study *Escherichia coli* adhesion to biomedical materials. Chem Eng Sci. 126:440–445.

Moreira JMR, Teodósio JS, Silva FC, Simões M, Melo LF, Mergulhão FJ. 2013. Influence of flow rate variation on the development of *Escherichia coli* biofilms.

Bioprocess Biosyst Eng. 36(11):1787–1796.

Norsker N-H, Barbosa MJ, Vermuë MH, Wijffels RH. 2011. Microalgal production — A close look at the economics. Biotechnol Adv. 29(1):24–27.

O'Neill ME. 1968. A sphere in contact with a plane wall in a slow linear shear flow. Chem Eng Sci. 23(11):1293–1298.

van Oss CJ. 1993. Acid-base interfacial interactions in aqueous media. Colloids Surfaces A Physicochem Eng Asp. 78(C):1–49.

van Oss CJ. 2008. The extended DLVO theory. In: Interface Sci Technol. Vol. 16. [place unknown]: Elsevier; p. 31–48.

Ozkan A. 2012. Development of a novel algae biofilm photobioreactor for biofuel production. [place unknown]: The University of Texas at Austin.

Ozkan A, Berberoglu H. 2013. Adhesion of algal cells to surfaces. Biofouling. 29(4):469–482.

Paul BK, Hires CL, Su YW, Chang CH, Ramprasad S, Palo D. 2012. A uniform residence time flow cell for the microreactor-assisted solution deposition of CdS on an FTO-glass substrate. Cryst Growth Des. 12(11):5320–5328.

Pereira MO, Kuehn M, Wuertz S, Neu T, Melo LF. 2002. Effect of flow regime on the architecture of a *Pseudomonas fluorescens* biofilm. Biotechnol Bioeng. 78(2):164–171.

Polimetacrilato de Metilo - Catalogo en linea - Materiales en pequenas cantidades para el diseno - Goodfellow.

Roosjen A, Boks NP, Van Der Mei HC, Busscher HJ, Norde W. 2005. Influence of shear on microbial adhesion to PEO-brushes and glass by convective-diffusion and sedimentation in a parallel plate flow chamber. Colloids Surfaces B Biointerfaces. 46(1):1–6.

Ruiz-Cabello FJM, Rodríguez-Valverde MA, Cabrerizo-Vilchez MA. 2011. Contact angle hysteresis on polymer surfaces: An experimental study. J Adhes Sci Technol. 25(16):2039–2049.

Rutter PR, Vincent B. 2018. Attachment mechanisms in the surface growth of microorganisms. 2nd Editio. New York: CRC Press.

Saffman PG. 1965. The lift on a small sphere in a slow shear flow. J Fluid Mech. 22(2):385–400.

Sharma MM, Chamoun H, Sarma DSHSR, Schechter RS. 1992. Factors controlling the hydrodynamic detachment of particles from surfaces. J Colloid Interface Sci. 149(1):121–134.

Sharma PK, Hanumantha Rao K. 2003. Adhesion of *Paenibacillus polymyxa* on chalcopyrite and pyrite: Surface thermodynamics and extended DLVO theory. Colloids Surfaces B Biointerfaces. 29(1):21–38.

Simões M, Pereira MO, Sillankorva S, Azeredo J, Vieira MJ. 2007. The effect of hydrodynamic conditions on the phenotype of *Pseudomonas fluorescens* biofilms. Biofouling. 23(4):249–258.

Soriano-Jerez Y, López-Rosales L, Cerón-García MC, Sánchez-Mirón A, Gallardo-Rodríguez JJ, García-Camacho F, Molina-Grima E. 2020. Long-term biofouling formation mediated by extracellular proteins in *Nannochloropsis gaditana* microalga

30

cultures at different medium N/P ratios. Biotechnol Bioeng. 118(3):1152–1165.

Stone L, Hastie D, Zigan S. 2019. Using a coupled CFD – DPM approach to predict particle settling in a horizontal air stream. Adv Powder Technol. 30(4):869–878.

Subramaniam S. 2013. Lagrangian-Eulerian methods for multiphase flows. Prog Energy Combust Sci. 39(2–3):215–245.

Talluri SNL, Winter RM, Salem DR. 2020. Conditioning film formation and its influence on the initial adhesion and biofilm formation by a cyanobacterium on photobioreactor materials. Biofouling. 36(2):183–199.

Tang Y, Valocchi AJ, Werth CJ, Liu H. 2013. An improved pore-scale biofilm model and comparison with a microfluidic flow cell experiment. Water Resour Res. 49(12):8370–8382.

Teodósio JS, Simões M, Alves MA, Melo LF, Mergulhão FJ. 2012. Setup and validation of flow cell systems for biofouling simulation in industrial settings. Sci World J. 2012.

Teodósio JS, Simões M, Melo LF, Mergulhão FJ. 2011. Flow cell hydrodynamics and their effects on E. coli biofilm formation under different nutrient conditions and turbulent flow. Biofouling. 27(1):1–11.

Touhami A, Nysten B, Dufrêne YF. 2003. Nanoscale Mapping of the Elasticity of Microbial Cells by Atomic Force Microscopy. Langmuir. 19:4539–4543.

Vadillo-Rodríguez V, Busscher HJ, Norde W, de Vries J, van der Mei HC. 2004. Relations between macroscopic and microscopic adhesion of *Streptococcus mitis* strains to surfaces. Microbiology. 150(4):1015–1022.

Vreeland V, Waite JH, Epstein L. 1998. Minireview—polyphenols and oxidases in substratum adhesion by marine algae and mussels. J Phycol. 34(1):1–8.

Yan H, Vosswinkel N, Ebbert S, Lipeme Kouyi G, Mohn R, Uhl M, Bertrand-Krajewski J-L. 2020. Numerical investigation of particles' transport, deposition and resuspension under unsteady conditions in constructed stormwater ponds. Environ Sci Eur. 32(1).

Yap B, Crawford S, Dagastine R, Martin G. 2016. Nitrogen deprivation of microalgae: effect on cell size, cell wall thickness, cell strength, and resistance to mechanical disruption. J Ind Microbiol Biotechnol. 43:1671–1680.

Zeriouh O, Reinoso-Moreno JV, López-Rosales L, Cerón-García MC, Sánchez-Mirón A, García-Camacho F, Molina-Grima E. 2017. Biofouling in photobioreactors for marine microalgae. Crit Rev Biotechnol. 37(8):1006–1023.

Zeriouh O, Reinoso-Moreno JV, López-Rosales L, Cerón-García MC, Sánchez Mirón A, García-Camacho F, Molina-Grima E. 2019. Assessment of a photobioreactor-coupled modified Robbins device to compare the adhesion of *Nannochloropsis gaditana* on different materials. Algal Res. 37:277–287.

Zeriouh O, Reinoso-Moreno JV, López-Rosales L, Sierra-Martín B, Cerón-García MC, Sánchez-Mirón A, Fernández-Barbero A, García-Camacho F, Molina-Grima E. 2017. A methodological study of adhesion dynamics in a batch culture of the marine microalga Nannochloropsis gaditana. Algal Res. 23:240–254.

Zhang Z, Chen Q. 2009. Prediction of particle deposition onto indoor surfaces by CFD with a modified Lagrangian method. Atmos Environ. 43(2):319–328.

Zhao H, Zhao Y. 2020. CFD-DEM simulation of pneumatic conveying in a horizontal

pipe. Powder Technol. 373:58–72.

Zhao Y, Ambrose RPK. 2019. Modeling dust dispersion and suspension pattern under turbulence. J Loss Prev Process Ind. 62:103934.

1
2
3
4
5
6
7
8
9
10
11
12
13
14
15
16
17
18
19
20
21
22
23
24
25
26
27
28
29
30
31
32
33
34
35
36
37
38
39
40
41
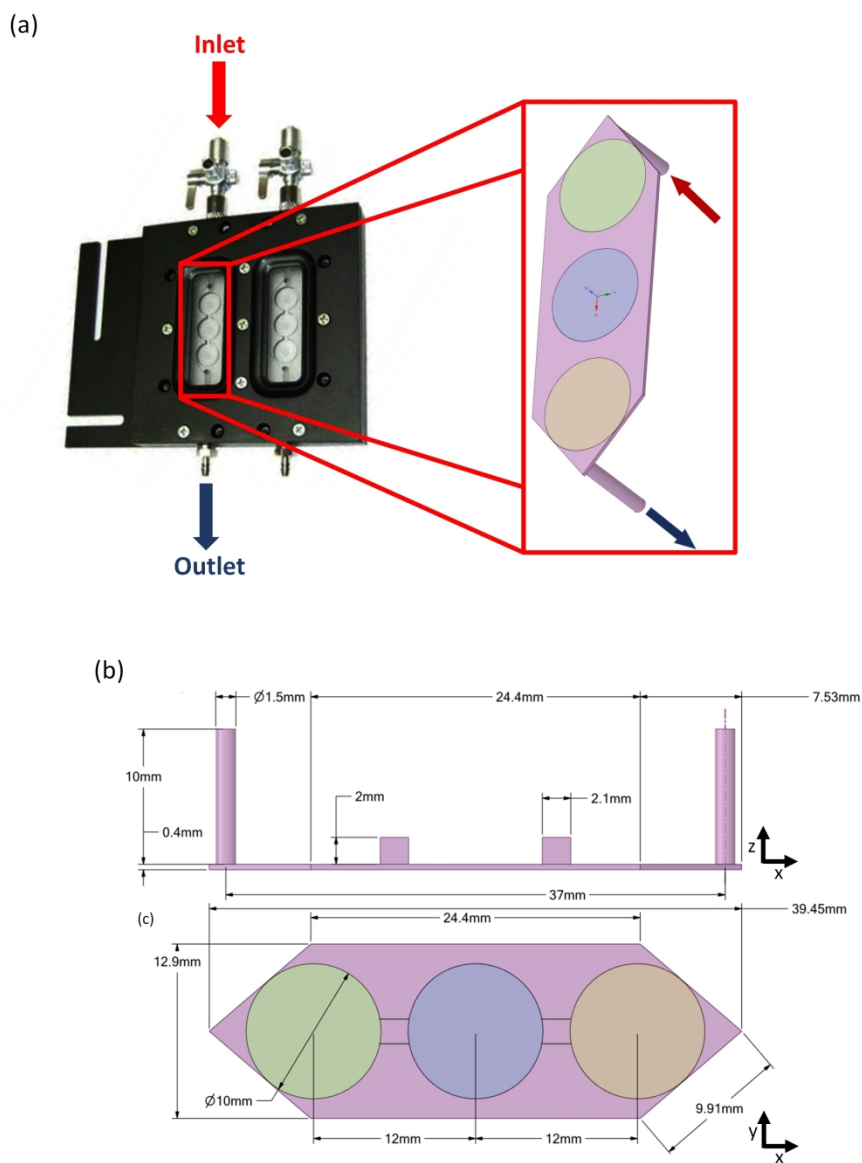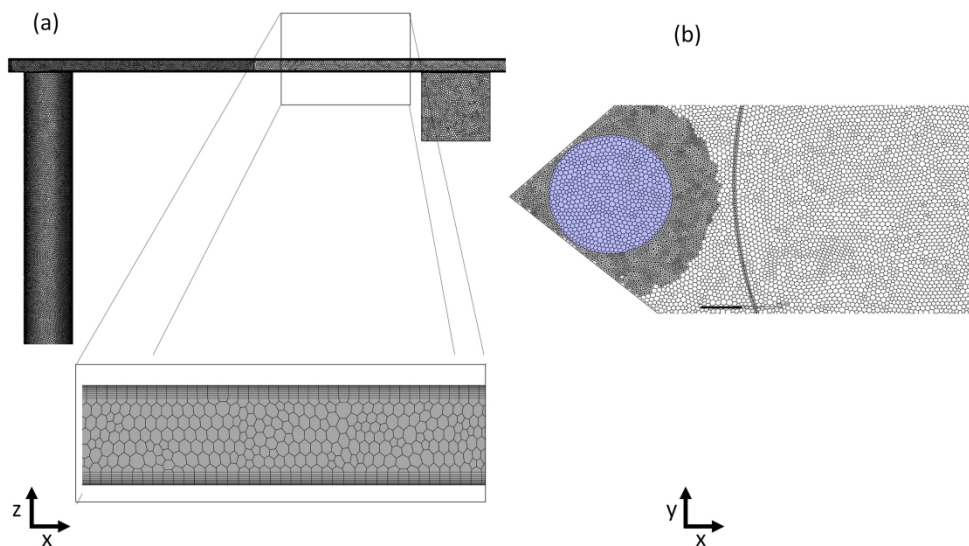42
43
44
45
46
47
48
49
50
51
52
53
54
55
56
57
58
59
60

1
2
3
4
5
6
7
8
9
10
11
12
13
14
15
16
17
18
19
20
21
22
23
24
25
26
27
28
29
30
31
32
33
34
35
36
37
38
39
40
41
42
43
44
45
46
47
48
49
50
51
52
53
54
55
56
57
58
59
60

Figure 1. a) Photograph of the FC271 flow cell; b) main dimensions from the side view (y-axis) and from the overhead view (z-axis).

214x281mm (330 x 330 DPI)

Figure 2. a) Detail of the mesh in the central x-z plane and detail of the mesh refinement on solid surfaces, (b) Mesh zoom at the flow cell entrance (x-y plane). Inlet channel is highlighted in blue.

253x158mm (330 x 330 DPI)

Normalized liquid velocity (U_f/U_0) profiles in the direction of y-axis
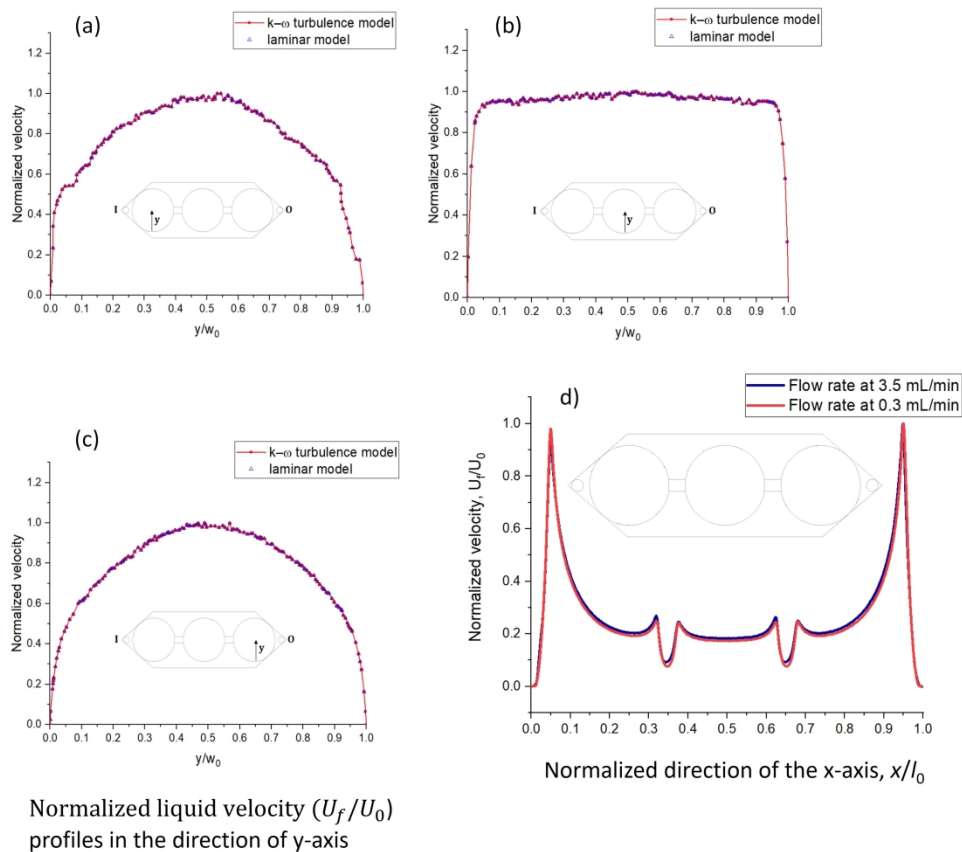
Figure 3. Normalized liquid velocity profile for the maximum flow rate (3.5 mL·min^{-1}) along an x-y line (z = 200 μm) in the dimensionless central transverse direction (see insets) for coupons located at: (a) the cell inlet, x = 12 mm; (b) the centre of the cell, x = 0 mm; (c) the cell outlet, x = -12 mm; and d) a comparison of the normalized liquid along a line in the x direction (z = 200 μm) for both flow rates assayed. The vertical dotted lines delimit the beginning and end of each coupon. In all cases, U_f is the point velocity of the fluid and U_0 is the maximum velocity reached at each flow, w_0 is the chamber width and l0 is the length.
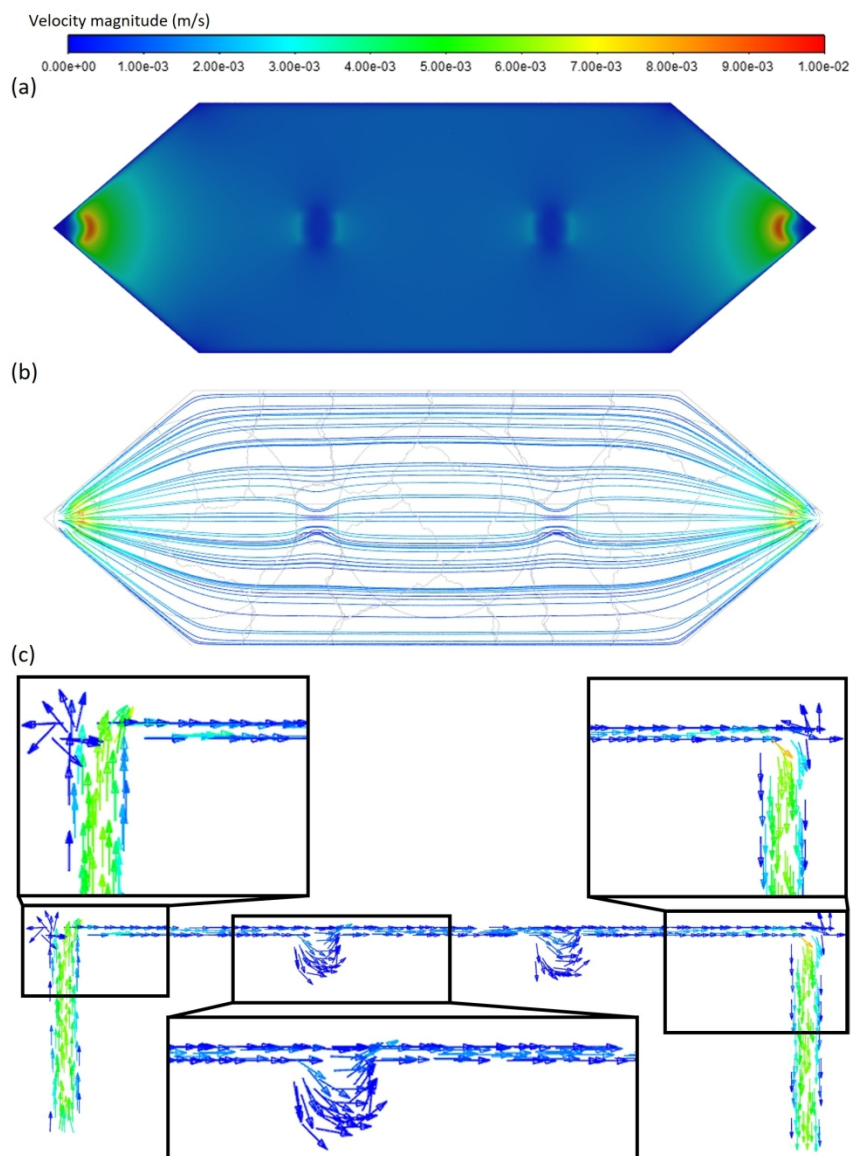
258x225mm (330 x 330 DPI)

Figure 4. Liquid velocity in the flow cell obtained in the simulations for a flow rate of 0.3 mL·min^{-1}; a) contour graph on an x-y plane (z = 200 μm), (b) flow lines and (c) vectors on a longitudinal x-z plane in the centre of the cell (y = 0 mm).
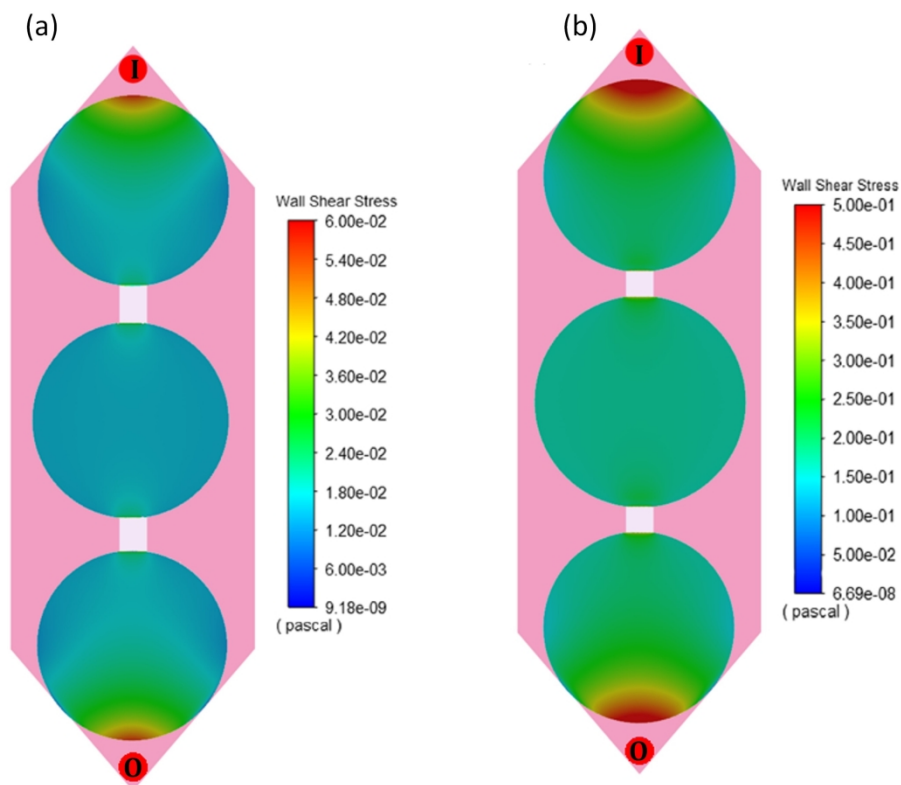
158x191mm (330 x 330 DPI)

Figure 6. Contour graphs of wall shear stress for the different coupons of the flow cell at (a) 0.3 mL·min^{-1} and (b) 3.5 mL·min^{-1}. I: inlet; O: outlet.
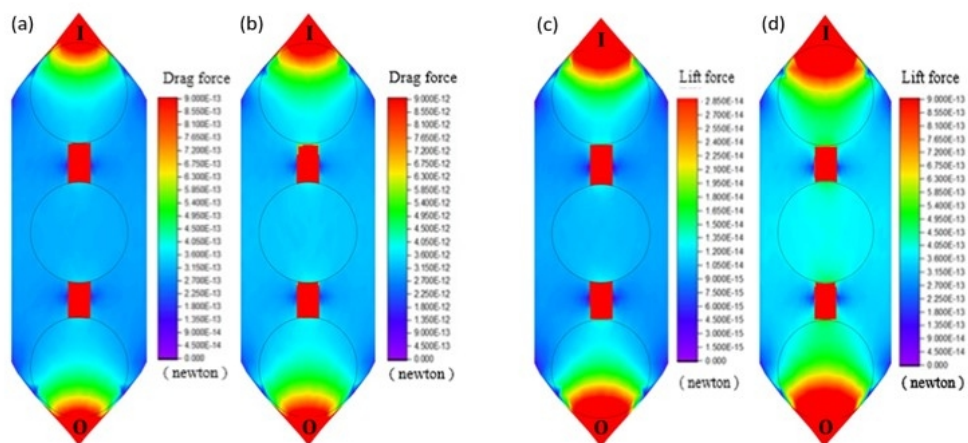
226x182mm (330 x 330 DPI)

Figure 7. Contour plots for the drag force on a plane that is 2 μm from the surface of the coupons at a flow rate of (a) 0.3 mL·min^{-1} and (b) 3.5 mL·min^{-1}; and the lift force at a flow rate of (c) 0.3 mL·min^{-1} and (d) 3.5 mL·min^{-1}; I: inlet, O: outlet.
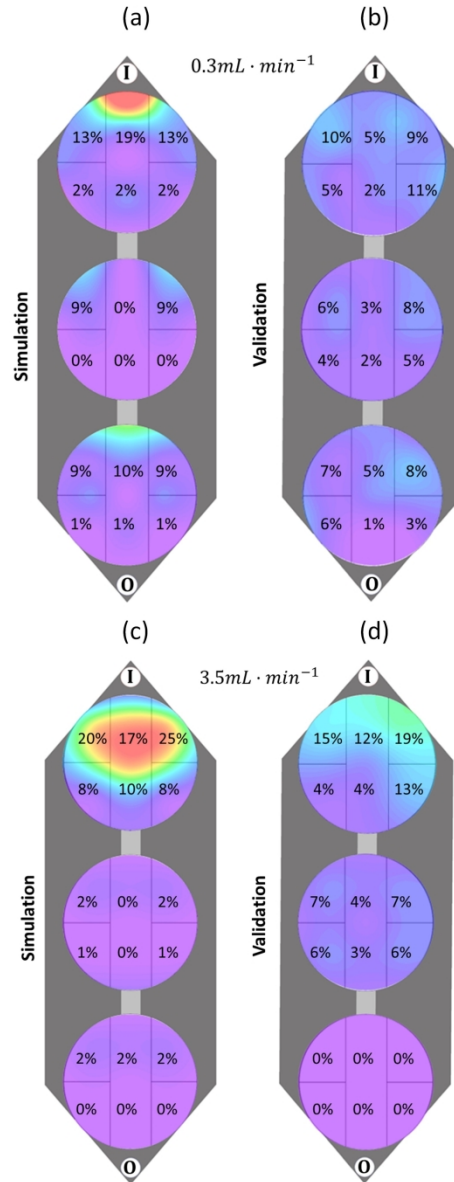
263x128mm (72 x 72 DPI)

Figure 8. Relative distribution of the adhered cells in 6 different zones of the three coupons in the flow cell for the a) simulation at 0.3 mL·min^{-1}, b) validation assay at 0.3 mL·min^{-1}, c) simulation at 3.5 mL·min^{-1}, and d) validation assay at 3.5 mL·min^{-1}. The validation results are the average of the measurements from the 5 replicate adhesion experiments.

129x315mm (330 x 330 DPI)

Table 1. Properties of the cells, liquid, and clean surfaces.

Material	Property	Value and units	Ref.
Sea water	ε	$68.5 \cdot 10^{-10}$ F·m^{-1}	Ellison et al. (1998)
Microalgae (*N. gaditana*)	a	$2 \cdot 10^{-6}$ m	Zeriouh et al. (2017)
Surface	λ	1 - 2 nm	Zeriouh et al. (2017)
Sea water	υ	$5 \cdot 10^{-11}$ m	Sharma & Hanumantha Rao (2003); Zeriouh et al. (2017)
Microalgae	ς_m	-6.6 mV	Zeriouh et al. (2017)
Surface	ψ_s	-6.92 mV	Zeriouh et al.(2017)
Microalgae	E_1	2 MPa	Touhami et al. (2003)
Surface	E_2	3 GPa	Goodfellow Inc.
Microalgae	v_1	0.5	Yap et al. (2016)
Surface	v_2	0.3	Goodfellow Inc.
Minimun cell-surface distance	d_0	$1,57 \cdot 10^{-10}$ m	Bos et al. (1999)

Table 2. Surface energy components γ obtained from Soriano-Jerez et al. (2020) and Zeriouh et al. (2017) : LW components to the apolar (LW forces) components; (+) and (-) refer to the electron acceptor and donor, respectively; m and s refer to the microalga and material surfaces, respectively; l represents the culture medium.

Surface properties $(\text{J}\cdot\text{m}^{-2})$			
	$\gamma_{s,l,m}^{LW}$	$\gamma_{s,l,m}^{+}$	$\gamma_{s,l,m}^{-}$
Medium (water) - l	$21.8 \cdot 10^{-3}$	$25.5 \cdot 10^{-3}$	$25.5 \cdot 10^{-3}$
Microalgae (*N. gaditana*) - m	0.034	$7.024 \cdot 10^{-4}$	0.048
Surface (PMMA) - s	0.0438	$6.5 \cdot 10^{-4}$	0.0277

Table 3. Results of the analysis of variance of the experimental cell adhesion extension. The factors considered were position of the coupon in the flow- cell (A), measuring position of the adhesion on the coupons (B), culture flow rate (C) and replica analyses (D). Only those interactions with statistical significance have been collected.

Principal effects	Sum of squares	*F*-ratio	*p*-value	Number of homogeneous groups
A: Coupon	0.0110032	72.29	0.0000	3
B: Measurement position	0.0102099	6.71	0.0000	7
C: Culture flow rate	0.0000279633	0.37	0.5456	1
D: Replica	0.0000686359	0.30	0.8249	1
Interactions				
AB	0.00570683	1.87	0.0054	
AC	0.00175394	11.52	0.0000	
BC	0.00351452	2.31	0.0031	
ABC	0.00468833	1.54	0.0407	

1
2
3
4
5
6
7
8
9
10
11
12
13
14
15
16
17
18
19
20
21
22
23
24
25
26
27
28
29
30
31
32
33
34
35
36
37
38
39
40
41
42
43
44
45
46
47
48
49
50
51
52
53
54
55
56
57
58
59
60

A. Cell culture.

Nannochloropsis gaditana B-3 species (Instituto de Ciencias Marinas de Andalucía (CSIC, Cádiz, Spain)) was cultured in a 13-L flat panel photobioreactor (Figure B) for 71 days (Figure B). Cultures were illuminated in 12h:12h light-dark cycles at 135 $\mu E \cdot s^{-1} \cdot m^{-2}$ (irradiance measured on the external surface of the PBR wall). Light was provided by a 12 uniformly distributed 26W fluorescent bulbs. The average temperature in the culture chamber was 25 ± 2 ºC. The culture medium was N-optimized ALGAL (Camacho-Rodríguez et al. 2013), which was formulated using pre-filtered and sterilized (in autoclave) Medierranean seawater
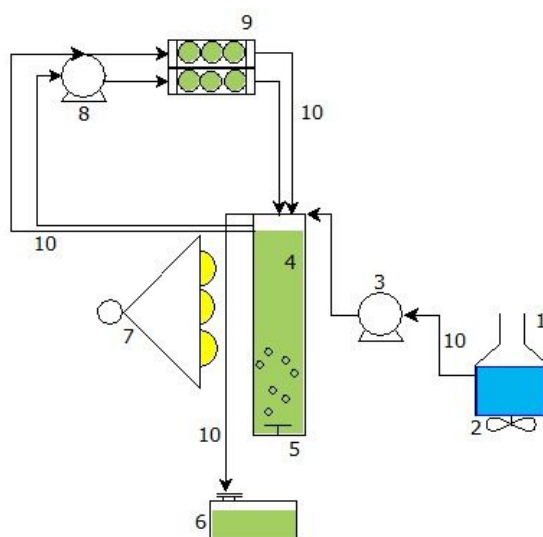

Figure A. Culture setup scheme and flow cell recirculation system. (1) Culture medium reservoir; (2) Magnetic stirrer; (3) Peristaltic pump; (4) Flat panel photobioreactor; (5) Sparger; (6) Harvest bottle; (7) Lighting system; (8) Multi-channel peristaltic pump; (9) Flow cell with three methacrylate coupons per channel; (10) Silicone tubes.

Kichou et al. 2021 **Supplementary material**

The PBR was operated discontinuously until day 30. Biomass concentration at t=30

days was 2.1 g·L^{-1}. From day 30, continuous culture mode was initiated (Figure B).

Culture medium was added at 1.3 L·day^{-1} and 0.5 L·day^{-1} of distilled water was also added

to compensate evaporation. A steady-state concentration of approx. 0.9 g·L^{-1} was

achieved. Culture gowth was monitored daily, measuring the relative cell concentration

by absorbance in a plate reader (SynergyMx, BioTek Instruments Inc., USA) at a

wavelength of 540 nm (Abs540). The relationship between biomass concentration and

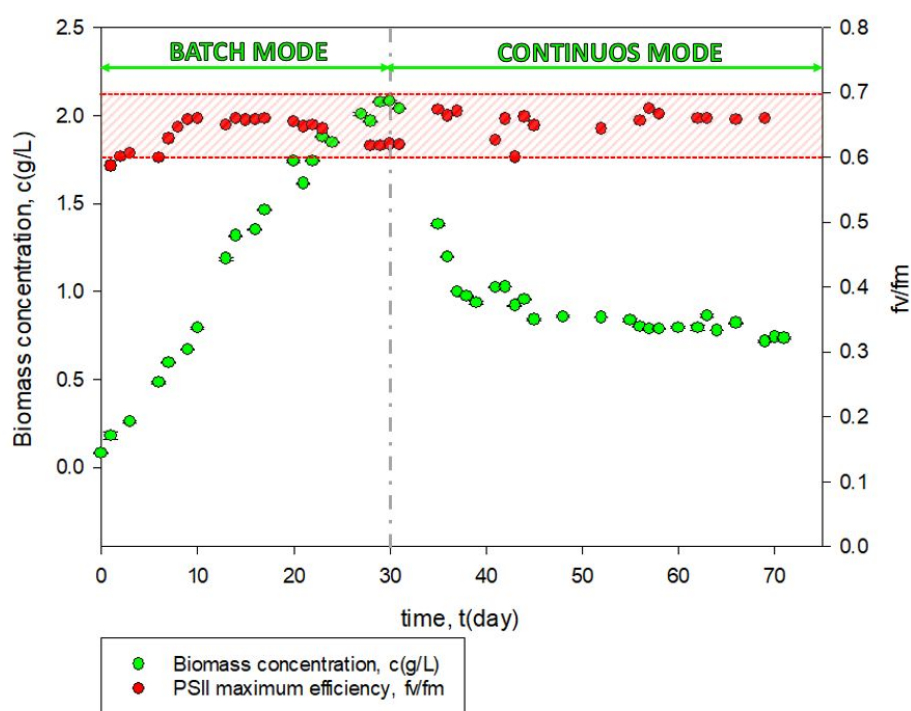absorbance was obtained from Soriano-Jerez et al. (2020).

Figure B. Evolution of cell concentration and *Fv* / *Fm* over time.

The photosynthetic health status of the culture was monitored with the maximum

photochemical performance of photosystem II (*Fv/Fm*) in a pulsed light fluorimeter

(PAM-2500 chlorophyll fluorometer, Heinz Walz GmbH, Effeltrich, Germany) (López-

Rosales et al. 2014). The *Fv/Fm* ranged between values of 0.6 and 0.67, which means that the health status of the culture remained considerably well throughout the culture.

B. Obtaining the adhesion maps

The adhesion maps were obtained by determining the cell fluorescence in 21 different positions of the coupons according to the distribution of Figure C.
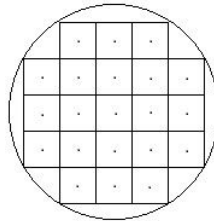

Figura C. Detail of the 21 fluorescence measurement positions on the coupon.

C. Adhesion force according to XDLVO model

The coupon-cell adhesion force depends on the separation distance between them. The properties of the clean methacrylate, according to the XDLVO model, cause a repulsive force with the cells of *N. gaditana* (red line in Figure D). However, as irreversible cell adhesion was observed on the surface of the methacrylate coupons after two hours of contact between the circulating suspension and the coupons, conditioned methacrylate properties were used. In this way, the forces were always of attraction between cells and coupons (blue line in Figure D).
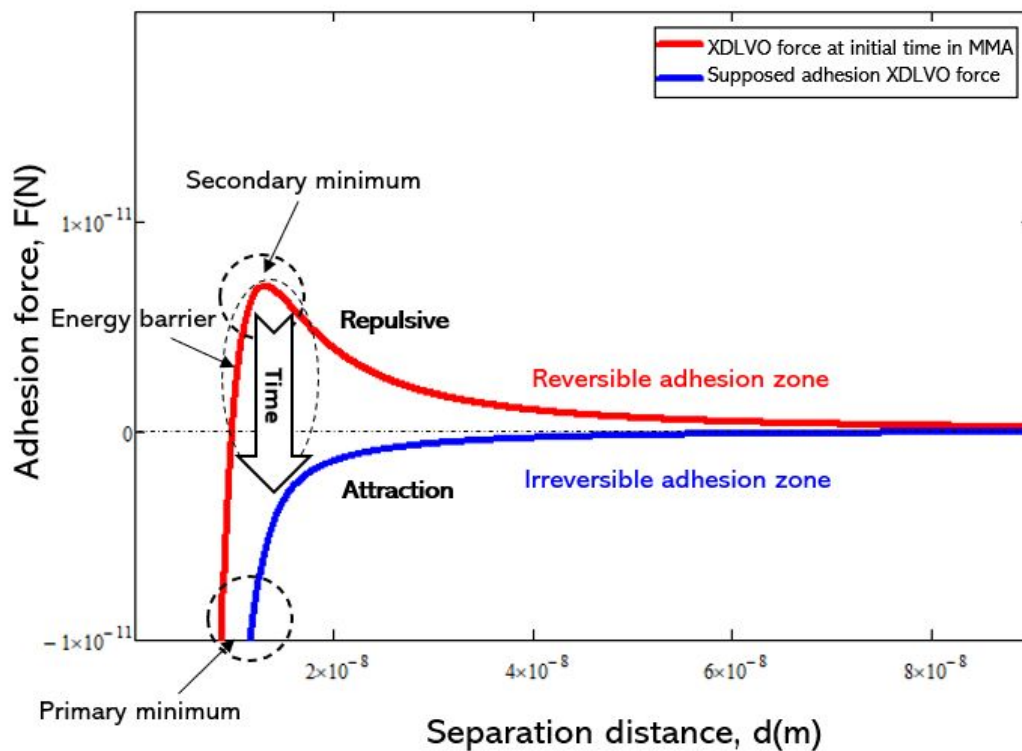
Figure D. Adhesion force with respect to the distance between *N. gaditana* and methacrylate coupons. The force used in the simulation corresponds to that of the irreversible or primary adhesion zone (conditioned surface).

D. Adhesion criterion

To determine whether or not a cell would adhere to the surface of the coupons, the force balance included in Figure E was considered (Henry 2018). To include this complex adherence criterion to the simulation, a UDF was used (Boundary Condition UDF). This UDF follows the scheme of Figure F: when a particle gets close enough to a wall, the UDF is executed and force balance result is read (it is calculated with another UDF). Then, calculations of the ratios 10, 11 and 12 are carried out. Three conditions establish that the particle would adhere. In this case, the UDF will abort the tracking of adhered particle and save the data in a file. Otherwise its trajectory continues to be calculated.

4

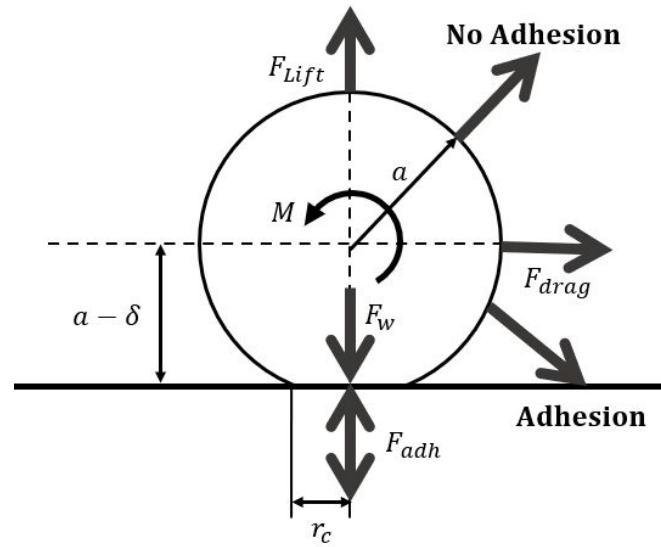**Figure E**. Force balance on a cell touching a solid surface (Adapted from Henry 2018).
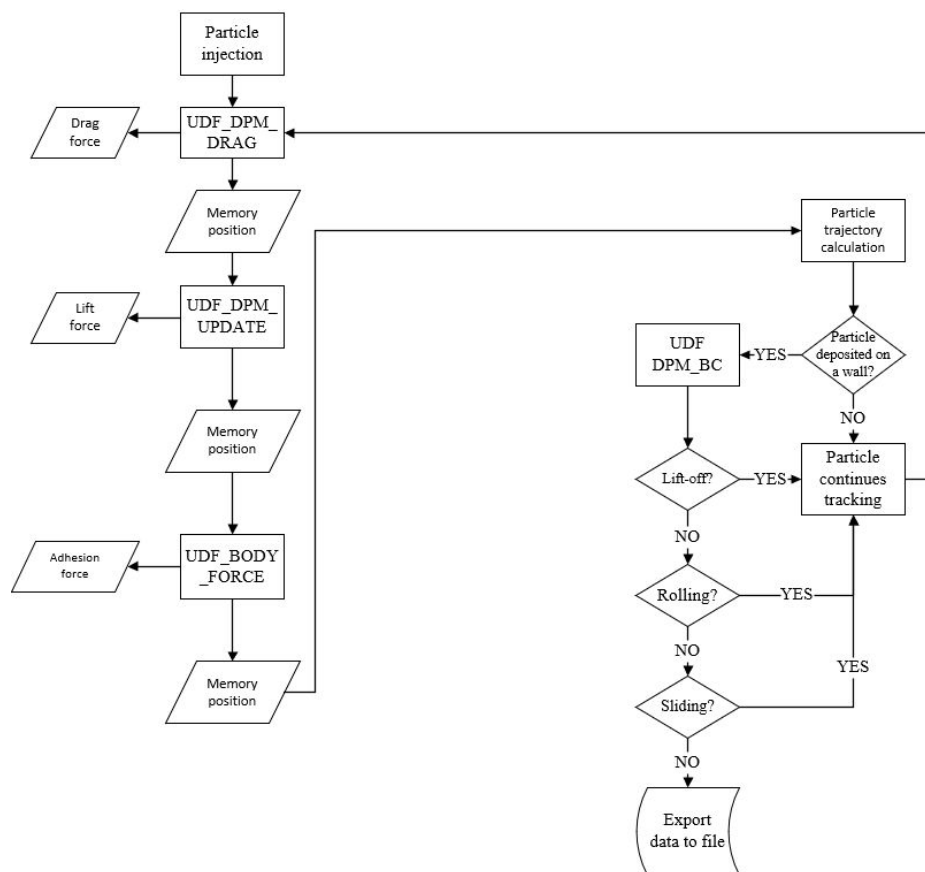

Figure F. Calculation diagram of the adhesion criterion of a particle on a solid surface according to the balance of forces and moments in Figure E.

5

The Boundary Condition UDF (DPM_BC) (Figure G) includes the different conditions outlined in Figure F.

a)
```c
DEFINE_DPM_BC(wall_xdlvo_model, p, t, f, f_normal, dim)
{
#if !RP_HOST
    if (p->type == DPM_TYPE_INERT)
    {
        if (P_USER_REAL(p, 5) == 0.)
        {
            /*****************************************Memory positions******************************************/
            P_USER_REAL(p, 6) = r0(P_DIAM(p), fabs(P_USER_REAL(p, 0))); /*Radio de contacto*/
            P_USER_REAL(p, 7) = P_POS(p)[0];
            P_USER_REAL(p, 8) = P_POS(p)[1];
            P_USER_REAL(p, 9) = P_POS(p)[2];
            P_USER_REAL(p, 10) = P_TIME(p);

            /*****************************************Force Balances******************************************/
            P_USER_REAL(p, 11) = P_USER_REAL(p, 3) / (P_USER_REAL(p, 0) + P_USER_REAL(p, 4)); // Lift-Off
            P_USER_REAL(p, 12) = P_USER_REAL(p, 1) / (ks * (P_USER_REAL(p, 0) + P_USER_REAL(p, 4) + P_USER_REAL(p, 3))); // Sliding
            P_USER_REAL(p, 13) = (0.5 * P_DIAM(p) * P_USER_REAL(p, 1) + P_USER_REAL(p, 6) * P_USER_REAL(p, 3)) / (P_USER_REAL(p, 6) * (P_USER_REAL(p, 0) + P_USER_REAL(p, 4))); // Rolling

                /*****************************************Adhesion criteria******************************************/
            if (pow(P_USER_REAL(p, 11), 2) < 1 && pow(P_USER_REAL(p, 12), 2) < 1 && pow(P_USER_REAL(p, 13), 2) < 1)
            {
                P_USER_REAL(p, 5) = 1.;
                P_USER_REAL(p, 14) = 1.;
                return PATH_ABORT; /*Adhesion*/
            }
            else
            {
                return PATH_ACTIVE; /*No adhesion*/
            }
        }
        else
        {
            return PATH_ABORT;
        }
    }
    else {
        return PATH_END;
    }
#endif
}
```

b)
```c
DEFINE_DPM_DRAG(particle_drag_force, Re, p)
{
    real w, drag_force;
    Thread* tcell = P_CELL_THREAD(p);
    cell_t c = P_CELL(p);
    real relVel[ND_3], dvtdn, fluidVel[ND_3];

    if (Re < 1)
    {
        drag_force = 18;
    }
    else if (Re < 20.0)
    {
        w = log10(Re);
        drag_force = 18.0 + 2.367 * pow(Re, 0.82 - 0.05 * w);
    }
    else
    {
        drag_force = 18.0 + 3.483 * pow(Re, 0.6305);
    }

    NV_D(fluidVel, =, C_U(c, tcell), C_V(c, tcell), C_W(c, tcell));      //assigning fluid velocity components to vector
    NV_VV(relVel, =, fluidVel, -, P_VEL(p));                            //calculating relative velocity of flow on particle by subtracting absolute particle velocity from fluid velocity
    dvtdn = NV_MAG(relVel);                                            //calculation of relative velocity magnitude
    P_USER_REAL(p, 1) = FD(drag_force, C_MU_L(c, tcell), P_RHO(p), P_DIAM(p), P_MASS(p), dvtdn); /*Drag force*/
    P_USER_REAL(p, 2) = dvtdn;
    return (drag_force);
}
```

c)
```c
DEFINE_DPM_SCALAR_UPDATE(liftforcegravity, cell, t, initialize, p)
{
    real relVel[ND_3], dvtdn, fluidVel[ND_3];
    real shearate;

        Thread* tcell = P_CELL_THREAD(p);
        cell_t c = P_CELL(p);

        shearate = C_STRAIN_RATE_MAG(c, tcell);/*Shear rate*/
        P_USER_REAL(p, 3) = FL(C_MU_L(c, tcell), P_DIAM(p), shearate, C_R(c, tcell), P_USER_REAL(p, 2)); /*Lift force*/
        P_USER_REAL(p, 4) = FG(P_MASS(p)); /*Weight*/

}
```

Kichouh et al. 2021   **Supplementary material**

d)
```
DEFINE_DPM_BODY_FORCE(xdlvo_force, p, i)
{
    int id = p->part_id;
    real distance = P_POS(p)[2];
    real a = P_DIAM(p) / 2;
    real force;

    if (distance < dmax  && distance > d0)
    {
        if (i == 2) force = FTOT(a, distance);
    }
    else if (distance < d0) {
        distance = d0;
        if (i == 2) force = FTOT(a, distance);
    }
    else {
        force = 0.0;
    }

    P_USER_REAL(p, 0) = force; /*XDLVO force*/
    return (force / P_MASS(p));
}
```

Figure G. User defined functions (UDFs). a) Wall adhesion criterion implemented in a user defined boundary function; b) UDF to compute particle drag coefficient (Ansys-Fluent 2003); c) UDF to update the lift and weight forces; d) UDF to compute XDLVO force.

E. Mesh sensitivity analisys

A sensitivity analysis for mesh elements was performed generating three meshes with different numbers of elements: mesh with 10^6 elements without inflation, mesh of $2 \cdot 10^6$ elements with inflation on the walls with an initial cell size of $2 \cdot 10^{-6}$ m and mesh with $5.4 \cdot 10^6$ elements with inflation in the walls with an initial cell size of $2 \cdot 10^{-6}$ m. As can be seen in Figure H, the first mesh does not adequately capture the liquid velocity at the cell inlet, although an adequate velocity profile was obtained in the rest of the flow cell.

Minimal differences were observed between the meshes of 2 and $5.4 \cdot 10^6$ elements in terms of velocity profiles along lines perpendicular to the surface of the coupons (z-direction) (Figure J). In the central coupons and closest to the outlet, the differences with the mesh with lower number of elements are more evident. In any case, the differences

7

were not important, despite the fact that the mesh of 10^6 elements did not implement an
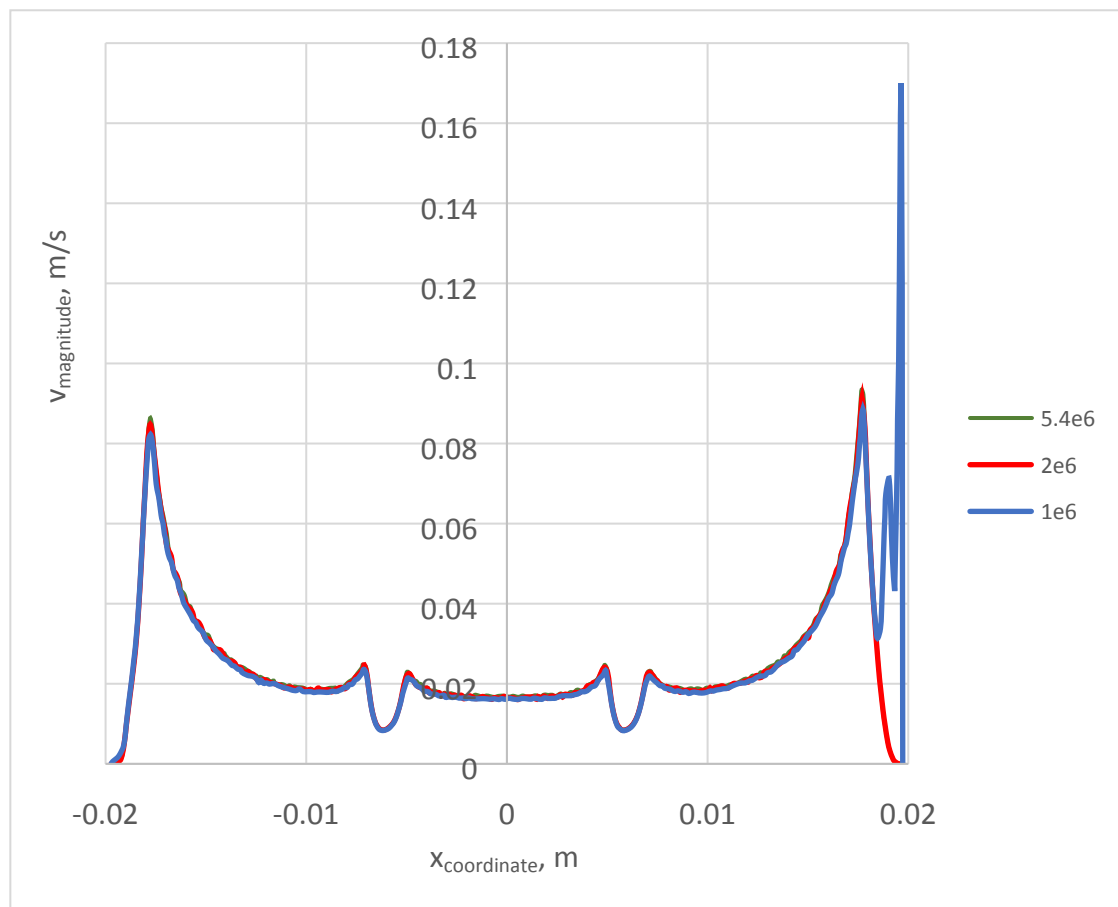
inflation layer to have better resolution near the walls.

Figure H. Velocity in the centre of the flow cell in the *x*-direction of the flow cell. $y = 0$ m, $z = 200\mu$m.

The differences are less evident in the velocity profiles along lines parallel to the

coupons (Figures K). Again, it is in the centre of the cell when the mesh with the lowest

resolution moves further away from the results obtained with the one with the highest
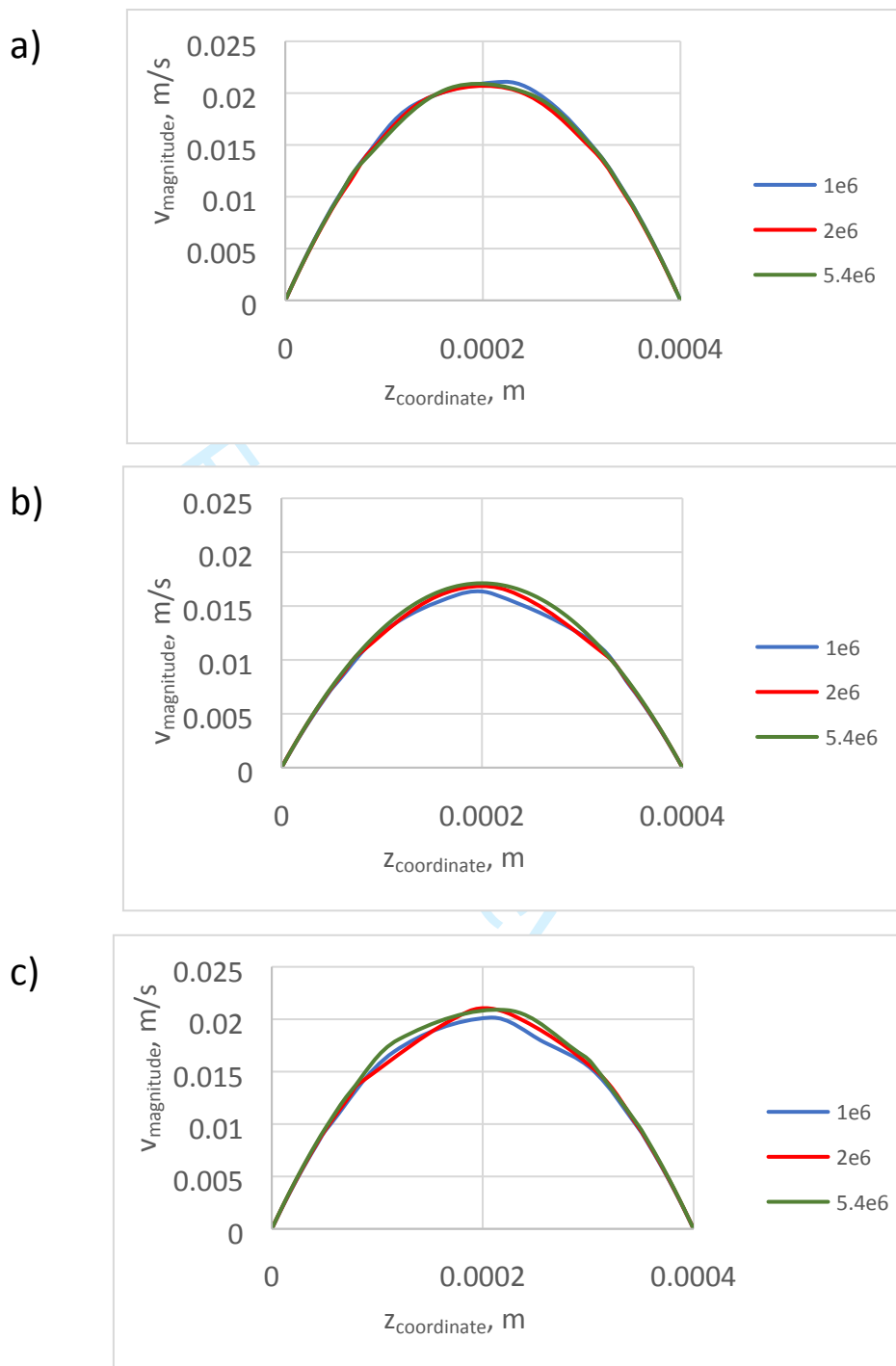
resolution.

Kichoub et al., 2021   **Supplementary material**

Figure J. Velocity magnitude in the centre of the flow cell along a line perpendicular to the centre of the coupons (*z* direction). a) *x* = 12 mm, *y* = 0 m; b) *x* = 0 mm, *y* = 0 m; c) *x* = -12 mm, *y* = 0 m.
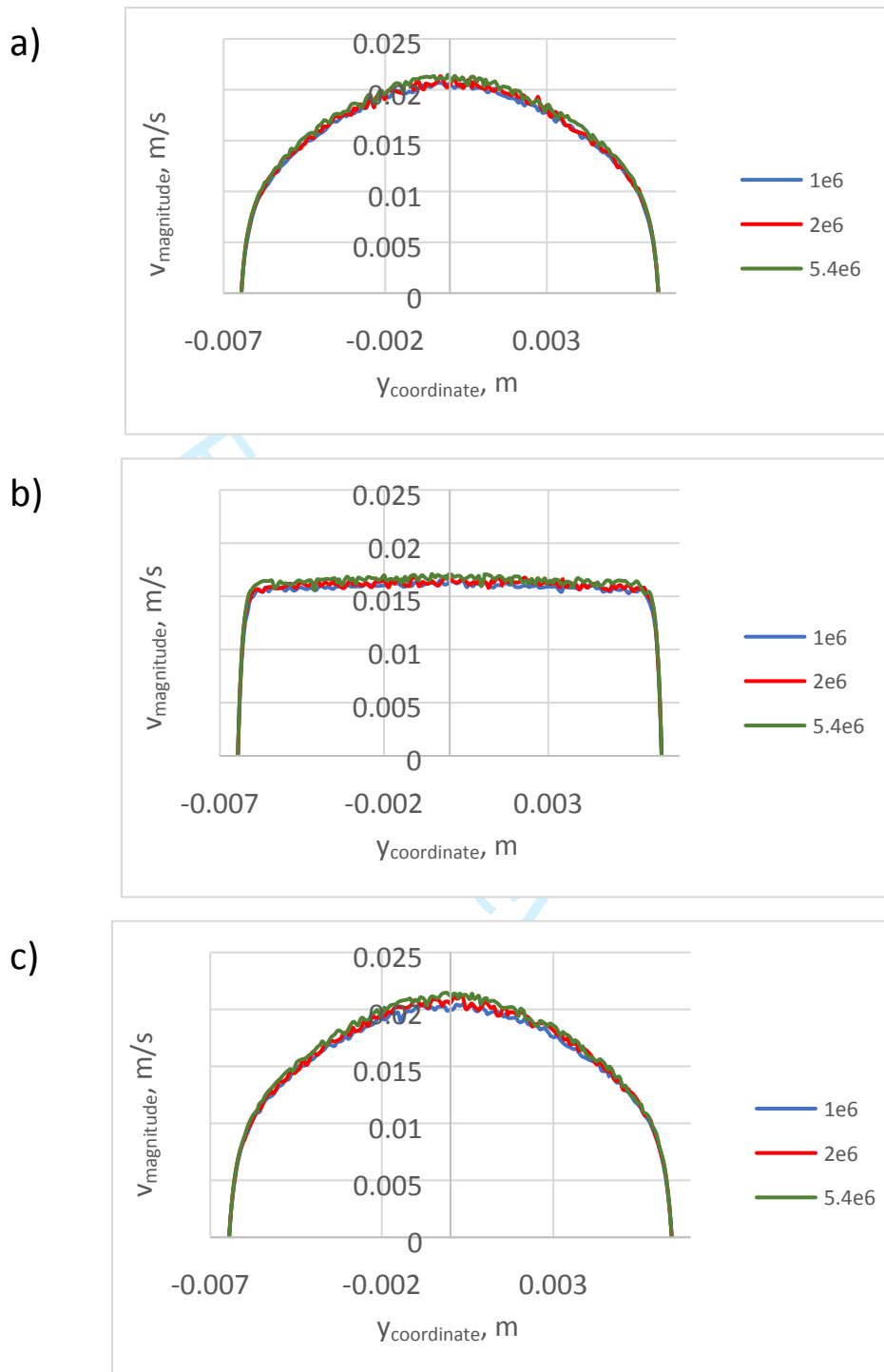
a)

b)

c)

Figure K. Velocity magnitude in the centre of the flow cell along a line perpendicular to the liquid flow (y direction). a) $x = 12$ mm, $z = 200$ μm; b) $x = 0$ mm, $z = 200$ μm; c) $x = -12$ mm, $z = 200$ μm.

Since the liquid velocity profiles in the vicinity of the walls are very similar with the three meshes, the wall shear stress values in the coupon walls are very similar with the

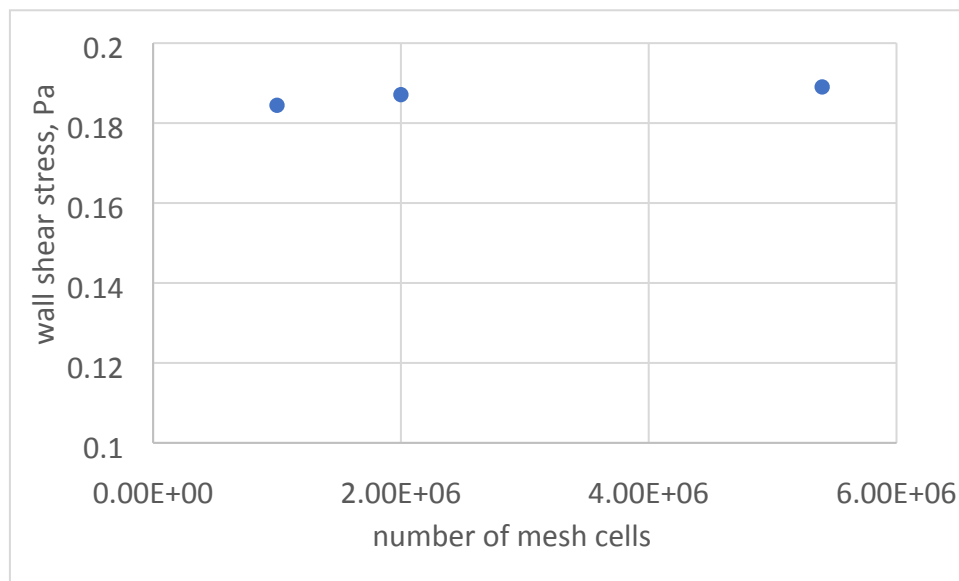three meshes, being practically indistinguishable between 2 and $5.4\cdot10^6$ elements (Figure

L).

Figure L. Average wall shear stress on the coupons plane ($z = 0$ m).

1
2
3
4
5
6
7
8
9
10
11
12
13
14
15
16
17
18
19
20
21
22
23
24
25
26
27
28
29
30
31
32
33
34
35
36
37
38
39
40
41
42
43
44
45
46
47
48
49
50
51
52
53
54
55
56
57
58
59
60

Kichouh et al., 2021 **Supplementary material**

Bibliography

Ansys-Fluent. 2003. Fluent 6.1 User's guide.

Camacho-Rodríguez J, Cerón-García MC, González-López C V., Fernández-Sevilla JM, Contreras-Gómez A, Molina-Grima E. 2013. A low-cost culture medium for the production of Nannochloropsis gaditana biomass optimized for aquaculture. Bioresour Technol. 144:57–66.

Henry C. 2018. Particle resuspension from complex surfaces: current knowledge and limitations. arXiv arXiv:180206448.

López-Rosales L, Gallardo-Rodríguez JJ, Sánchez-Mirón A, Cerón-García MDC, Belarbi EH, García-Camacho F, Molina-Grima E. 2014. Simultaneous effect of temperature and irradiance on growth and okadaic acid production from the marine dinoflagellate *Prorocentrum belizeanum*. Toxins (Basel). 6(1):229–253.

Soriano-Jerez Y, López-Rosales L, Cerón-García MC, Sánchez-Mirón A, Gallardo-Rodríguez JJ, García-Camacho F, Molina-Grima E. 2020. Long-term biofouling formation mediated by extracellular proteins in *Nannochloropsis gaditana* microalga cultures at different medium N/P ratios. Biotechnol Bioeng. 118(3):1152–1165.